Experiments Towards Mitigation of Motional Heating in Trapped Ion Quantum Information Processing

by Amy Greene
S.B., Physics and EECS, M.I.T. 2014
Submitted to the
Department of Electrical Engineering and Computer Science
in Partial Fulfillment of the Requirements for the Degree of
Master of Engineering in Electrical Engineering and Computer Science
at the
Massachusetts Institute of Technology
February 2016

Author .....
Department of Electrical Engineering and Computer Science
February 27, 2016

Certified by .....
Isaac Chuang
Professor of Physics, Professor of Electrical Engineering
Thesis Supervisor

Certified by .....
Jeremy Sage
MIT Lincoln Laboratory Technical Staff
Thesis Supervisor

Certified by .....
John Chiaverini
MIT Lincoln Laboratory Technical Staff
Thesis Supervisor

Accepted by .....
Dr. Christopher Terman
Chairman, Masters of Engineering Thesis Committee

Experiments Towards Mitigation of Motional Heating in Trapped Ion Quantum Information Processing

by

Amy Greene

Submitted to the Department of Electrical Engineering and Computer Science
on February 27, 2016, in partial fulfillment of the
requirements for the degree of
Master of Engineering in Electrical Engineering and Computer Science

Abstract

Trapped ions are a promising candidate for the implementation of quantum information processing. Techniques have already been developed for working with small systems of trapped-ion qubits; scalability is the biggest remaining challenge. One of the major scalability obstacles faced by trapped ions is an anomalous motional heating which limits the fidelity of two-qubit gates. It has been demonstrated that cleaning a gold trap chip via ion milling reduces the heating rate by two orders of magnitude [1]. However, it remains unclear why ion milling causes a much more dramatic improvement than similar cleaning techniques such as plasma cleaning, which only reduces the heating rate by a factor of 4 [2]. Understanding this difference will provide insight into the source of the anomalous heating noise.

In this work, we investigate the mechanism by which ion milling reduces the heating rate by cleaning niobium traps with a ex-situ ion milling followed by plasma cleaning. We find that the resulting reduction in the heating rate is consistent with that obtained from plasma cleaning alone. This, combined with a recent result from the ex-situ milling of gold traps [3], suggests that some component of the improvement mechanism is material-based.

Additionally, we present our work on the design and testing of a small resonator board used to deliver a high RF voltage to the trap chip. This board, made with off-the-shelf components, represents a more scalable alternative to the helical resonators which are commonly used for this purpose.

Thesis Supervisor: Isaac Chuang
Title: Professor of Physics, Professor of Electrical Engineering

Thesis Supervisor: Jeremy Sage
Title: MIT Lincoln Laboratory Technical Staff

Thesis Supervisor: John Chiaverini

Title: MIT Lincoln Laboratory Technical Staff

Acknowledgments

I owe a huge debt of gratitude to the ion trapping group at MIT Lincoln Laboratory. They have taken me in and succored me, and though some of my efforts have been useful, they certainly don't pay back all of the time and effort they have granted me. Coming here, I have been inspired. I have learned much about what it means to be a good scientist and member of scientific team, and I leave hoping to pursue a Ph.D in this field. In some ways this may be the highest compliment a student can pay to her teachers, and they have justly earned it.

To Jeremy Sage and John Chiaverini, thank you for your guidance and supervision. Thank you for your support when things didn't work, and for all of that time spent chasing mysterious factors of 2. Thank you also for the hiking books and music recommendations. Maybe I'll try watching The Wire now that I'll have a bit of spare time.

I cannot thank Robert McConnell enough for all of his hands-on guidance in the lab. Robert, I hope that someday I will be able to match your skill in finding the right allen wrench. I'm glad that your hard coffee addiction never wore off on me, despite all the time we spent working together. Hopefully some of your experimental skills did.

Colin Bruzewicz has always been quick with a witty word or a helpful explanation. Your enthusiasm for atomic physics is heady and contagious, and I am glad that you shared it with me.

Many thanks to Ike Chuang for taking me on as an advisee. Your advice has always been illuminating and insightful.

Several other individuals at MIT LL have been invaluable during this process. I especially wish to thank Peter Baldo for all of his instruction and assistance with trap fabrication. I have very fond memories of my time spent in ELab. Thanks also to Peter Murphy, Vladimir Bolkhovsky and Lee Mailhiot for their experience and kindness, to Chris Galbraith for his advice on RF systems, and to Eric Dauler for his help wrangling with the administrative side of the VI-A program.

I am so fortunate to have met you all!

Contents

List of Figures

List of Tables

Chapter 1

Introduction

The logic of quantum mechanics is different from that of classical systems, and this allows for new computational possibilities. Certain problems that are computationally difficult using the logic of classical computing may be solved exponentially faster using quantum information processing devices. The jury is still out on exactly how large this class of problems is, but several of the algorithms already developed could have a huge impact on our society. The classic example is Shor's algorithm [4], used to factor the product of two prime numbers in $O(logN)^3$ time. Using classical algorithms, this problem still takes exponential time to solve, and modern computer security is largely based on the assumption that such factoring is computationally difficult. Implementing Shor's algorithm on a sufficiently large quantum computer would overturn modern cryptography.

The possibilities are impressive, but the construction of quantum information processing devices is a challenge. Though quantum mechanics describes the underlying nature of reality, it tends to wash out to 'classical' behavior in most systems that we interact with. (This is why we develop classical intuition, and why quantum mechanics seems so strange).To find systems that exhibit quantum behavior we must seek out extremely small systems, isolate them from environmental effects and control them with extreme precision. Without an exquisite degree of isolation and control, quantum bits (qubits) will quickly lose their computational state, a phenomenon known as 'decoherence'. Meeting these demands taxes the limits of modern technology.

Just as the transistor revolutionized classical computing, we are currently searching for a scalable hardware implementation for quantum computing. There are several systems that are vying to become the 'transistor of quantum information processing'. Each implementation has its own strengths and struggles. Today, the most promising candidates are trapped ions, superconducting Josephson junctions, neutral atoms, and quantum dots.

In 1996, the physicist David DiVincenzo proposed a set of minimal requirements for the developing quantum hardware [5]. These criteria have become a standard against which potential qubit implementations are assessed:

1. **A scalable system with well-characterized qubits:** A physical qubit must be a well-understood system that can be approximated as having two energy levels. To be useful, quantum computing systems will need thousands to millions of physical qubits.

2. **The ability to initialize the qubits to a simple state:** Computation requires that registers be initialized to a known value before the start of an algorithm. Additionally, quantum error correction requires a continuous supply of qubits in the $|0\rangle$ state.

3. **Decoherence times that are much longer than the gate operation time:** $\frac{\text{Decoherence time}}{\text{Gate time}}$ roughly determines the number of operations that can be completed during the course of a computation. This ratio must be high for useful computation to be performed.

4. **A universal set of quantum gates:** Certain operations can be more easily implemented in a given qubit modality than others. The set of gate operations that can be realized in a potential hardware system must be sufficient to perform arbitrary computations.

5. **A qubit-specific measurement capability:** Quantum computation is only useful if the results can be read out. This requires the ability to measure specific qubits.

1.1 Trapped Ion QIP

Trapped ions are one of the most promising candidates for implementing quantum information processing. Since ions have an electric charge, they can be trapped in an electromagnetic field generated by certain electrode geometries. Qubits can be stored in their stable electronic states, and they can be controlled through laser pulses and the Coulomb interaction between nearby ions. Trapped ions already fulfill almost all of the DiVincenzo requirements; scalability is the only significant outstanding challenge.

1. **Well-characterized qubits:** Two internal energy states of the ion serve as the $|0\rangle$ and $|1\rangle$ states of the qubit. Several different pairs of energy levels may be used, but the two most common choices are two hyperfine sublevels of an ion's electronic ground state (known as a hyperfine qubit) and the electronic ground state combined with a metastable excited state (known as an optical qubit). The work described in this thesis utilizes the $^2S_{\frac{1}{2}}$ and $^2D_{\frac{5}{2}}$ states of $^{88}Sr^+$.

2. **Initialization:** Initialization of the qubits used in this experiment consists of preparing the ion in the ground electronic state and cooling it to its motional ground state using optical pumping and laser cooling techniques.

3. **Long decoherence times relative to gate times:** For trapped-ion systems, single-qubit gates take about 1-10 μs, and two-qubit gate times of 10-100 μs have been achieved [6]. This compares favorably to the achievable coherence times in trapped ion systems, which is up to 50 seconds [6].

4. **Universal set of gates:** The C-NOT gate and the set of single-qubit operations form a universal set of gates for quantum computing. C-NOT gates have been already been performed with trapped ions using lasers [7, 8], as have single-qubit operations.

5. **Measurement:** The electronic state of ions can be detected via laser interrogation. (A more detailed description of trapped ion measurement is provided later in this work.)

1.2 Thesis Questions

In trapped-ion quantum computing, two-qubit gates are mediated by the Coulomb interaction, and they use the motion of the ion to transfer information. In other words, two-qubit gates depend on the motional states of the ion. Unfortunately, these motional states aren't very stable in the presence of electric field noise. At the right frequency, electric field fluctuations in the trapping potential couple to the ions' harmonic motion and increase their motional energy state. This heating places a practical limit on the development of high-fidelity multi-qubit gates.

Noise will be present in any system, but the observed heating rates correspond to a noise level which is several orders of magnitude greater than we expect to see. Currently, the heating rate is thought to be caused by fluctuating patch potentials on the surface of the ion trap, but the cause of the patch potentials is unknown. If the source of this anomalous heating can be identified, then it can likely be improved. For this reason, this electric field noise is currently the subject of much investigation.

Outside of operating at cryogenic temperatures [9], electrode surface cleaning is the only method discovered thus far which reduces the anomalous heating rate. By far, the biggest reduction was achieved in an experiment that used ion milling, a cleaning technique routinely used in microfabrication. In this experiment, the NIST ion trapping group was able to achieve a hundred-fold reduction in the heating rate of a gold trap [1]. They saw a correlation between the heating rate improvement and the removal of hydrocarbons from the trap surface, and it seemed that these hydrocarbons were causing the anomalous heating. However, when a different experiment removed hydrocarbons through plasma cleaning niobium traps, the heating rate was only reduced by a factor of 4 [2]. A previous study has shown that the heating rate of niobium traps exhibits dependencies that closely match those seen with gold traps [10]. This suggests that ion milling reduces the heating rate through an additional mechanism, beyond hydrocarbon removal. Understanding this mechanism could be key for solving the anomalous heating rate problem.

Ion milling and plasma cleaning both remove surface adherents by bombarding

the surface with other particles; in ion milling these other particles are ions, while in plasma cleaning they are the atoms, molecules, ions, electrons, free radicals, metastables, and photons of the plasma. The biggest difference between ion milling and plasma cleaning lies in the energy of these particles. The ions used in the ion milling work had kinetic energies of 2 keV, while those in the plasma cleaning experiment had only a few eV. Where plasma cleaning with a reactive species gently removes hydrocarbons, ion milling uses enough energy to blast off material indiscriminately. In addition to removing adherents, ion milling might be restructuring the surface of the material. This is supported by an ex-situ ion milling experiment [3], which found ion milling a trap and re-exposing it to air (and thus hydrocarbons) still improves the heating rate by an order of magnitude.

To test for surface rearrangement from ion milling, we try augmenting the plasma cleaning treatment with a prior ex-situ ion milling. As mentioned above, plasma cleaning will remove hydrocarbons without affecting the surface material. If ion milling causes some advantageous surface restructuring, that change will persist after the trap is re-exposed to air. Subsequent in-situ plasma cleaning would remove the hydrocarbons introduced by re-exposure, revealing any changes in the surface structure. If the combined cleaning procedure causes a stronger reduction in the heating rate than plasma cleaning alone, it would be a strong indication that ion-milling is causing beneficial surface restructuring.

Specifically, this thesis asks the following question: if a trap chip is cleaned via ex-situ ion milling followed by plasma cleaning, is the subsequent reduction in the anomalous heating rate greater than that obtained from plasma cleaning alone? Answering this question is a step towards addressing a major scalability issue faced by trapped ion quantum information processing; the answer will improve our understanding of the anomalous heating and will inform future efforts to mitigate its effects.

1.3 Thesis Approach and Hypothesis

To answer this question, we took advantage of the ion-trapping and plasma cleaning equipment already used by our group, and we constructed an ex-situ ion milling chamber capable of mimicking the milling procedure used in [1]. We take a Nb trap chip and clean it with ex-situ milling and then in-situ plasma cleaning, taking heating rate measurements at each stage in the process. We compare the resulting heating rates to those seen in our previous plasma-cleaning experiment [2].

Our hypothesis is that ion milling does indeed have an improvement mechanism beyond removing hydrocarbons, and that this mechanism which will cause ex-situ milling followed by plasma cleaning to result in a greater reduction in the anomalous heating rate than would plasma cleaning alone.

In addition to presenting our investigation of cleaning techniques, a portion of this thesis also describes our solution to a technology-related scalability issue. Creating systems with thousands of trapped ions will require large trap structures with many electrodes, and the electronics that control these electrodes will need to be small and easily constructed. However, one of the key pieces of electronic equipment does not meet these requirements: the helical resonators commonly used to deliver high-voltage radio-frequency (RF) signals to certain trap electrodes are bulky and must be carefully custom-built. We describe the development of an alternative resonator circuit which fits on a small PCB board and can be assembled from off-the-shelf components.

1.4 Contribution and Structure of Thesis

The work described in this thesis takes advantage of experimental equipment which has been previously assembled; we stand on the shoulders of giants. The ion-trapping apparatus and heating rate analysis scripts were developed by Jeremy Sage and John Chiaverini, while Robert McConnell constructed the in-situ plasma cleaning device which we have used. This work makes three primary contributions:

- The design and assembly of an ex-situ ion milling chamber
- An experimental study on the heating rate reduction from ex-situ milling followed by plasma cleaning
- The design and implementation of a compact resonator board made with off-the-shelf components

The body of this thesis is organized in two parts. We begin by providing a theoretical background to trapped ion quantum information processing. First we explain the fundamentals of strontium ion qubits, followed by a discussion of some of the nuances of the ion traps we use (actually called Paul traps) and how these affect the behavior of trapped ions. We also describe the anomalous heating in greater detail. Later chapters discuss our experimental setup and results. We describe our ion-trapping apparatus and technique for measuring the heating rate, and end by presenting the results obtained from testing our resonator circuit and from our combined cleaning technique. These topics are grouped as follows:

- **Chapter 2:** Fundamentals of Sr^+ qubits
- **Chapter 3:** Introduction to Paul traps
- **Chapter 4:** Overview of anomalous heating
- **Chapter 5:** Description of ion-trapping apparatus
- **Chapter 6:** Methodology of heating rate measurements
- **Chapter 7:** Demonstration of more-scalable resonator circuit
- **Chapter 8:** Heating rate reduction from ex-situ ion milling combined with plasma cleaning

Chapter 2

Sr^+ as a Qubit

In the work described in this thesis, strontium atoms are photoionized, trapped in a linear Paul trap and cooled to the motional ground state for use in studies of anomalous heating. This chapter describes the fundamentals of Sr^+ as a qubit, while subsequent chapters provide some theoretical background to Paul traps and anomalous heating.

In the previous chapter, we introduced the idea that physical qubits must possess the following properties: they must possess well-defined energy levels that can be used to approximate a two-state system, we must be able to prepare them in some initial state and we must be able to read out their state. Here, we take an in-depth look at how the $^{88}Sr^+$ qubit satisfies those requirements. This discussion provides a background which is necessary for understanding the experimental portion of this work. This section is organized as follows:

- **Section 2.1: Energy Levels** We begin with a discussion of the energy levels of the $^{88}Sr^+$ ion. In addition to defining the $|0\rangle$ and $|1\rangle$ states of the qubit, this section describes the transitions in Sr^+ and neutral strontium which are used in this work. This section also introduces the motional energy levels of trapped strontium, which are critical to an understanding of the anomalous motional heating.

- **Section 2.2: State Preparation** This section discusses how we initialize $^{88}Sr^+$

to the $|0\rangle$ state. There are three techniques involved in this process: Doppler cooling, resolved sideband cooling and optical pumping. All three are treated in detail.

- **Section 2.3: State Measurement** Finally, we explain how we measure the state of our ions. There are two forms of state measurement that are important for this work: distinguishing between the $|0\rangle$ and $|1\rangle$ states, and measuring the motional energy level. Both of these measurements are used when measuring the heating rate.

2.1 Energy Levels

To understand $^{88}Sr^{+}$ as a qubit, it is necessary to have some familiarity with the ion's lowest-lying energy levels. While we do our best to make the ion behave as a two-state system, the ion is ultimately a real system with an infinite number of energy levels. Most of these can be ignored, but not all. We break this section into two parts: a description of the relevant internal states of the ion, and a discussion of its motional states and how they affect spectroscopy. The internal state of the ion is also known as the atomic state or as the electronic state, and refers to the state of its electrons. These states are used to encode the $|0\rangle$ and $|1\rangle$ states of the qubit. The motional energy states correspond to the kinetic energy of the ion, and are used in two-qubit gates for trapped ions. Understanding the motional energy levels of the ion is key for an understanding of the anomalous heating.

2.1.1 Internal Energy Levels

Before discussing the atomic structure of Sr^{+}, let us briefly describe the energy levels of neutral strontium used to create the ion. The transitions used to photoionize Sr are shown in Figure 2-1, and the corresponding wavelengths and transition linewidths are shown in Table 2.1. In the $(4d^2 + 5p^2)^1D_2$ level, two electrons are excited such that each is bound, but their combined energy is greater than the first ionization

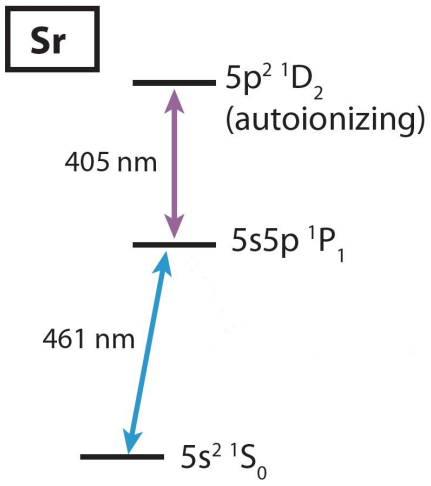

Figure 2-1: Energy levels relevant for the photoionization of neutral strontium

Transition	Wavelength	$\frac{\Gamma}{2\pi}$	$\tau = \frac{1}{\Gamma}$
${}^1S_0 \rightarrow {}^1P_1$	460.8620 nm [11]	32 MHz	5.0 ns [12]
${}^1P_1 \rightarrow {}^1D_2$	405.2 nm [13]	260 GHz	0.6 ps [13]

Table 2.1: Relevent transitions of neutral strontium.

potential. This state is autoionizing; one electron falls to the ground state and the other is ejected.

Strontium is a group II metal, which means that it has two valence electrons. After we pop off an electron to create Sr^+, we are left with a particle that has a hydrogen-like structure. This is to our advantage because hydrogen-like structures are fairly well understood. In Figure 2-2, we show the lowest energy levels of Sr^+. All of these states are used in our experiment. The wavelengths and linewidths of the relevant transitions can be found in Table 2.2.

The ${}^2D_{\frac{3}{2}}$ and ${}^2D_{\frac{5}{2}}$ states can decay only through dipole-forbidden transitions,

Transition	Wavelength	$\frac{\Gamma}{2\pi}$	$\tau = \frac{1}{\Gamma}$
${}^2S_{\frac{1}{2}} \rightarrow {}^2P_{\frac{1}{2}}$	421.6707 nm [11]	20.22 MHz	7.87 ns [14]
${}^2S_{\frac{1}{2}} \rightarrow {}^2P_{\frac{3}{2}}$	407.886 nm [11]	22.77 MHz	6.99 ns [14]
${}^2S_{\frac{1}{2}} \rightarrow {}^2D_{\frac{5}{2}}$	674.02559 nm [15]	0.41 Hz	390 ms [16]
${}^2D_{\frac{3}{2}} \rightarrow {}^2P_{\frac{1}{2}}$	1091.7860 nm [11]	1.52 MHz	105 ns [14]
${}^2D_{\frac{5}{2}} \rightarrow {}^2P_{\frac{3}{2}}$	1033.01 nm [11]	1.38 MHz	115 ns [14]

Table 2.2: Relevant transitions of Sr^+.

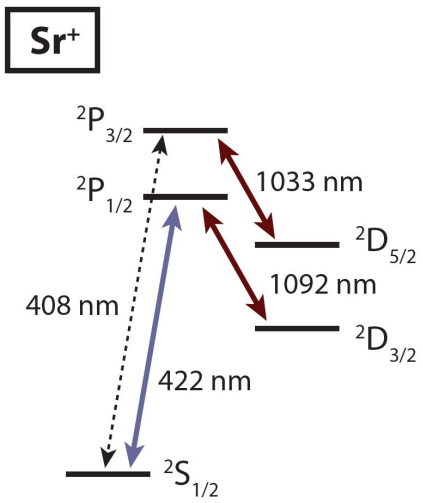

Figure 2-2: Lowest-lying energy levels of Sr^+

giving them a long lifetime. This long lifetime makes the ${}^2S_{\frac{1}{2}} \rightarrow {}^2D_{\frac{5}{2}}$ transition an ideal candidate for quantum information processing; the ${}^2S_{\frac{1}{2}}$ state serves as the $|0\rangle$ state of the qubit, and the ${}^2D_{\frac{5}{2}}$ as the $|1\rangle$ state. The 674nm laser which performs this transition is sometimes referred to as the 'probe' laser. When we want to reset the qubit back to the $|0\rangle$ state we use 1033nm laser; it mixes the ${}^2D_{\frac{5}{2}}$ state with the ${}^2P_{\frac{3}{2}}$, which rapidly decays back to the ground state. This process is known as 'quenching'.

The 20 MHz linewidth of the ${}^2S_{\frac{1}{2}} \rightarrow {}^2P_{\frac{1}{2}}$ transition allows it to be used to perform Doppler cooling, which is a key part of initial state preparation. This transition is also used for readout after the ion has been prepared in a superposition of the $|0\rangle$r and $|1\rangle$ states. Both of these processes are described in later sections.

The ${}^2P_{\frac{1}{2}}$ state usually decays to the ground state, but not always. With a branching ratio of $\frac{1}{13}$ it decays to the metastable ${}^2D_{\frac{3}{2}}$ state. If left unremedied, this would prevent efficient cooling and state preparation. Instead, we use the 1092 nm laser to 'repump' the ion from the ${}^2D_{\frac{3}{2}}$ state back to ${}^2P_{\frac{1}{2}}$.

The ${}^2D_{\frac{5}{2}}$ state is also used to realize sub-Doppler cooling of the ion through resolved sideband cooling, and in the state preparation process of optical pumping. Repumping with the 1092 nm light during these processes allows many cooling cycles to be performed rapidly.

A summary of these energy levels and their uses is given in Table 2.3.

State:	Uses:
$^2S_{\frac{1}{2}}$	Ground state; qubit $\|0\rangle$
$^2D_{\frac{3}{2}}$	Sometimes the ion decays here and needs to be repumped out
$^2D_{\frac{5}{2}}$	qubit $\|1\rangle$, also used in resolved sideband cooling and optical pumping
$^2P_{\frac{1}{2}}$	state measurement and Doppler cooling
$^2P_{\frac{3}{2}}$	Returning qubit to ground state from $^2D_{\frac{5}{2}}$

Table 2.3: Summary of lowest-lying energy levels and their uses

2.1.2 Motional Energy Levels

For reasons explained in the next chapter, the electric potential that the trapped ion experiences can be approximated as a 3D harmonic oscillator potential, with different frequencies along each axis. Let us denote these frequencies as ω_{axis}. Accordingly, the energy spacing of the motional energy levels along each axis is $\hbar\omega_{axis}$. The resulting motion is known as 'secular motion' for historical reasons. Due to the design of our trap, the frequencies of secular motion along the two radial axis of the trap are in the 4-5 MHz range, while the secular motion along the axis parallel to the RF electrodes has a much lower frequency of about 1 MHz. In our experiments, we assess the ion's heating rate by measuring the energy state of the secular motion along this third axis; in this work it is often referred to just as the 'axial frequency' (for reasons related to the trap geometry), or simply as the 'trap frequency' of the ion. The average energy level of the axial motion is denoted '$\bar{\mathrm{n}}$', with corresponding average energy $\bar{\mathrm{E}} = \bar{\mathrm{n}}\hbar\omega_{axial}$.

In addition to addressing the internal energy states of the ion, photons can also impart momentum to the ion, exciting its motional states. An ion in the $^2S_{\frac{1}{2}}$ state with n = 0 can be excited to the $^2D_{\frac{5}{2}}$, n = 0 state with light at a frequency we'll denote here as f_0, but it can also be excited to the $^2D_{\frac{5}{2}}$, n = 1 state with light at the frequency $f_0 + \hbar\omega$. Similarly, an ion in the $^2S_{\frac{1}{2}}$ state with n = 1 can be excited to the $^2D_{\frac{5}{2}}$, n = 0 state with light at the frequency $f_0 - \hbar\omega$. These secondary transitions are weaker than the primary 'carrier' transition by a factor of the Lamb-Dicke parameter η. Tertiary transitions at $f_0 \pm 2\hbar\omega$ are weaker than the carrier transition by a factor of η^2, etc. These higher-order transitions are known as the 'sidebands', though the term

often refers only to the first-order sidebands at $f_0 \pm \hbar\omega$.) The sideband at $f_0 + \hbar\omega$ is called the 'blue sideband', since it shifted up in frequency. Similarly, the sideband at $f_0 - \hbar\omega$ is the 'red sideband' because it is shifted down in frequency. These sideband transitions are used in resolved sideband cooling and also in measuring the heating rate.

2.2 State Preparation

When ions are initially loaded in the trap, they have kinetic energies on the order of tens of meV. To use ions for quantum information processing, they must be cooled to the ground motional state. We undertake this cooling in two stages. Initially, the ion is Doppler cooled with the 422 nm laser, until the ion has $\bar{n} = \frac{1}{2}(\frac{\Gamma}{\omega} - 1)$, where Γ is the linewidth of the transition (typically tens of MHz) and ω is the trap frequency [17]. Then resolved sideband cooling is used to cool the ion to $\bar{n} < 1$. During the cooling process, sometimes the ion falls into an undesirable Zeeman sublevel of the ground state in which it cannot be addressed by our cooling beams. We use optical pumping to return the ion back to the preferred sublevel of the ground state.

Here we seek to convey a theoretical understanding of these three state preparation techniques. Later, in Chapters 5 and 6, we provide a discussion of how these techniques are realized in our experiment.

2.2.1 Doppler Cooling

There are many excellent reviews of Doppler cooling in the literature [17, 18, 19, 20]; here a brief intuition-based explanation is presented.

When an ion is hit by a photon at the frequency of an internal transition, it absorbs the photon and receives a small momentum kick in the direction the photon was traveling. When the ion spontaneously decays back to the ground state, it emits a photon of the same frequency in a random direction. In doing so the ion again receives a small momentum kick, this time in a random direction. Over many absorption-emission cycles, the ion experiences a net increase in momentum away from the photon

source.

When an ion is moving towards a laser, the frequency of light it sees is shifted up in frequency via the Doppler effect. If the incident light is tuned slightly below the resonant frequency, an ion moving towards the laser sees resonant photons and has its momentum reduced through the process described above. However, if the ion is not moving towards the laser, it experiences no momentum change.

During Doppler cooling, we hit a trapped ion with a beam of red-detuned 422 nm light. As the ion undergoes harmonic motion within the trap, its momentum is reduced every time it moves towards the beam source. This cools the ion. If the incident laser has a component along all three principal axis of the bound ion's motion, the ion is cooled along all three axes. However, Doppler cooling cannot cool the ion below the level of the randomized momentum kicks caused by the isotropic reemission of absorbed photons. In order to reach $\bar{n} \approx 0$ the ion must be cooled further, using resolved sideband cooling.

It is worth noting that the 422 nm laser can also heat the ion if its frequency is tuned slightly above the resonance. The mechanism for this is the same as Doppler cooling, only now the ion only 'sees' the photons if it is moving away from the beam. The blue-detuned 422 nm photons give the ion momentum kicks in the same direction that it is moving, causing it to gain motional energy until it is lost from the trap. For this reason, we always keep the 422 nm laser slightly red-detuned from resonance.

2.2.2 Resolved Sideband Cooling

Detailed descriptions of sideband cooling can be found in [21, 22, 23, 20, 24].

In resolved sideband cooling, the ion is cycled from $^2S_{\frac{1}{2}} \rightarrow {}^2D_{\frac{5}{2}} \rightarrow {}^2P_{\frac{3}{2}} \rightarrow {}^2S_{\frac{1}{2}}$ such that energy is dissipated. For this process, it is crucial that the linewidth of the transition is small compared to the trap frequency. First, a coherent pulse of 674 nm tuned to the red sideband causes the internal state to change from $^2S_{\frac{1}{2}} \rightarrow {}^2D_{\frac{5}{2}}$ as the motional occupation number decreases by one. A pulse from the 1033 nm laser then transitions the ion to $^2P_{\frac{3}{2}}$ without changing its motional state. Soon, the ion falls back to the ground state through spontaneous emission. Since the trap frequency

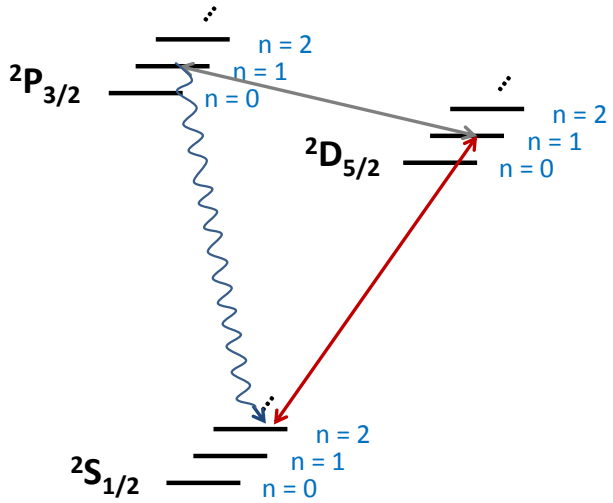

Figure 2-3: Diagram depicting resolved sideband cooling.

is much greater than the recoil from the emitted photon, the motional state will predominately remain the same - one occupational level lower than it had been at the start of the cycle. This process is depicted in Figure 2-3.

Though the ion could be allowed to spontaneously decay from the $^2D_{\frac{5}{2}}$ level, the long lifetime of the state would make the process impractical. For this reason, we instead couple with the 1033 nm laser to the $^2P_{\frac{3}{2}}$ state, which decays much more rapidly. We have also chosen to pulse our sideband cooling beams, instead of leaving them on continuously. If the 1033 nm laser was left on continuously, the AC Stark effect would cause the energy of the $^2D_{\frac{5}{2}}$ level to shift as the amplitude of the 1033 nm laser fluctuates. Since the $^2S_{\frac{1}{2}} \rightarrow ^2D_{\frac{5}{2}}$ transition is so narrow, this would be problematic. Pulsing the beams so that the 1033 nm and 674 nm lasers are never on at the same time avoids this problem.

2.2.3 Optical Pumping

Though $^{88}Sr^+$ has no hyperfine splitting, applied magnetic fields will split energy levels into M_J sublevels via the Zeeman Effect. Since it is difficult to perfectly isolate the experimental system from fluctuating background magnetic fields, we instead

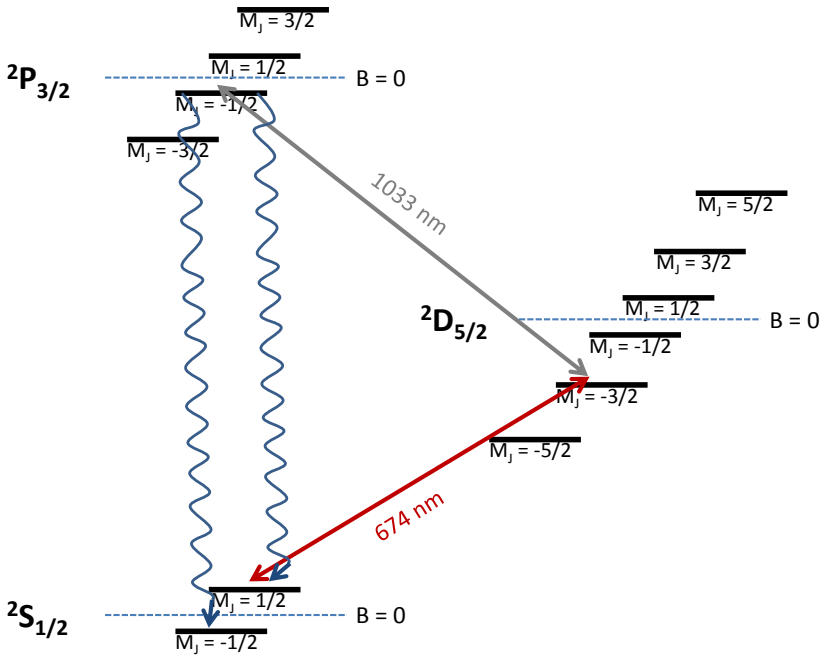

Figure 2-4: Diagram of optical pumping. Here, the dashed lines labelled 'B = 0' represent where the M_j sublevels would be in the absence of an applied magnetic field.

intentionally create a $\sim$5 Gauss magnetic field so we can control the M_J sublevel of the ion. Though we are predominantly able to keep the ion in the lowest M_J sublevel of each state, when the ion spontaneously decays from the $^2P_{\frac{3}{2}}$ state to ground it can fall back into the wrong $M_J = \frac{1}{2}$ sublevel. When the ion is in the wrong M_J sublevel, the 674 nm probe pulse is no longer resonant with the desired transition.

We use spectroscopic optical pumping to pump the ion back into the $M_J = -\frac{1}{2}$ ground state, as shown in Figure 2-4. The 674 nm laser is red-detuned from the carrier frequency and used to excite the $^2S_{\frac{1}{2},M_J=\frac{1}{2}} \rightarrow ^2D_{\frac{5}{2},M_J=-\frac{3}{2}}$ transition. The 1033 nm laser then raises the ion to the $^2P_{\frac{3}{2},M_J=-\frac{1}{2}}$ state. When the ion spontaneously decays back to the $^2S_{\frac{1}{2}}$ state, it will land in either of the ground states. The red-detuned 674nm beam affects the ion if it is in $^2S_{\frac{1}{2}}$, but not if it is in the desired $^2S_{\frac{1}{2},M_J=-\frac{1}{2}}$ state, so the process can be repeated until the ion has an arbitrary high probability of being in the right ground state.

2.3 State Measurement

State measurement is another critical aspect of a trapped ion experiment. Though the details of state measurement in our apparatus are laid out in Chapter 5 and Chapter 6, this section provides a brief theoretical groundwork for understanding those measurements. Here we are specifically concerned with two measurements: a measurement of the internal state which distinguishes between the $|0\rangle$ and $|1\rangle$ states, and a measurement of the motional state of the ion.

2.3.1 Internal State Measurement

The internal state of the ion can be discerned via laser interrogation. When the ion is in the $^2S_{\frac{1}{2}}$ state, illumination from the 422 nm will cause the ion to cycle on the $^2S_{\frac{1}{2}} \rightarrow ^2P_{\frac{1}{2}}$ transition. Each time the ion decays from the $^2P_{\frac{1}{2}}$ state, it scatters a photon, and these photons can be detected. For this reason, the $^2S_{\frac{1}{2}}$ state is sometimes referred to as the 'bright' state. When ion is in the $^2D_{\frac{5}{2}}$ state, the 422 nm does not address an transition and the ion remains 'dark'. When the ion is prepared identically and in

many trials and the heating rate is measured, this technique can be used to determine the probability with which the ion is in the $^2D_{\frac{5}{2}}$. In this work, we use this technique when performing spectroscopy.

2.3.2 Motional State Measurement

When the ion is cooled to $\bar{n} \lesssim 1$, the relative height of the red and blue sidebands of the $^2S_{\frac{1}{2}} \rightarrow ^2D_{\frac{5}{2}}$ transition can be used to determine $\bar{n}$. When the ion is in a thermal state, the probability of making a blue or red sideband transition is shown below:

$$P_{rsb} = \sum_{n=0}^{\infty} P_n \sin^2(\frac{\Omega_{n,n-1}t}{2}) \tag{2.1}$$

$$\begin{aligned} P_{bsb} &= \sum_{n=1}^{\infty} P_n \sin^2(\frac{\Omega_{n,n+1}t}{2}) \\ &= \sum_{n=0}^{\infty} P_{n-1} \sin^2(\frac{\Omega_{n-1,n}t}{2}) \\ &= \frac{\bar{n}}{1+\bar{n}} \sum_{n=0}^{\infty} P_n \sin^2(\frac{\Omega_{n-1,n}t}{2}) \end{aligned} \tag{2.2}$$

where P_n is the probability of being in the nth level of axial motion and $P_n = (\frac{\bar{n}}{1+\bar{n}})^n(\frac{1}{1+\bar{n}})$ and $\Omega_{n,n-1} = \Omega_{n-1,n}$ is the Rabi frequency of the corresponding transition. It follows that $\bar{n}$ can be extracted from $\frac{P_{bsb}}{P_{rsb}}$:

$$\frac{P_{bsb}}{P_{rsb}} = r = \frac{\bar{n}}{1+\bar{n}} \tag{2.3}$$

$$\bar{n} = \frac{r}{1-r} \tag{2.4}$$

The ratio $r = \frac{P_{bsb}}{P_{rsb}}$ can be found by taking the ratio of the heights of the red and

blue sidebands from a typical frequency scan.

Chapter 3

The Paul Trap

Because they have a charge, ions can be trapped by a suitable electric field. First implemented by Wolfgang Paul in the 1950s (for which he received the 1989 Nobel Prize), this traps have come to be known as 'Paul traps'. The original Paul traps had a 3D geometry consisting of long pieces of metal [25]. Since then, they have been adapted into 2D surfaces that can be microfabricated [26].

A basic knowledge of Paul traps is useful for understanding the work presented in this thesis. Paul traps are well described in literature [25, 27, 28], but in this chapter their salient points are briefly highlighted. Section 3.1 explains why RF fields are nececary for trapping ions, and Section 3.2 provides a mathematical description of how a linear quadropole RF potential can be used to trap an ion. This section also explores how the quadopole trapping potential gives rise to two kinds of motion: a high-amplitude, low-frequency 'secular' motion and high-frequency, low-amplitude micromotion.

Though thorough mathematical descriptions of ion traps are useful, they are also unweildy and difficult to perform for non-ideal trap geometries. In Section 3.3, we present the pseudopotential approximation which is often used to gain a more intuitive understanding of the ion trap and to simulate complex trap geometries. The ion traps used in this work fall into that category; we use linear surface electrode traps (SETs) which can be microfabricated on a 2D surface. Section 3.4 provides an introduction to these traps.

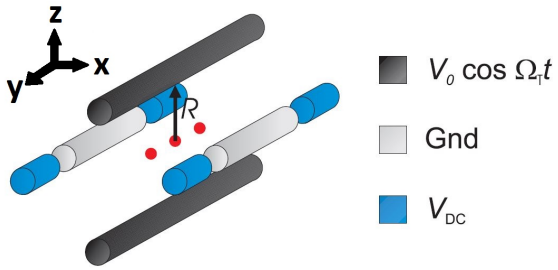

Figure 3-1: Diagram of a 3D Paul trap [29]

3.1 Trapping in an RF Field

Here, we describe why an RF component of the the potential is needed to trap an ion. In an ideal vacuum, there are no static potentials that will trap an ion along all 3 spatial axes. This is known as Earnshaw's Theorem, and it arises from one of Maxwell's equations: $\nabla\ \mathbf{E} = \frac{\rho}{\epsilon_0}$. The electric field is the negative derivative of the electric potential ($\mathbf{E} = -\nabla\Psi$), which means that when there is no charge density (as in a vacuum), $\nabla^2\Phi = \nabla\ \mathbf{E} = 0 = \frac{\partial E_x}{\partial x} + \frac{\partial E_y}{\partial y} + \frac{\partial E_z}{\partial z}$. This implies that $\frac{\partial E_x}{\partial x}$, $\frac{\partial E_y}{\partial y}$, and $\frac{\partial E_z}{\partial z}$ cannot all have the same sign. Physically, this means that static electric fields can create saddle points, but not minima.

However, if the field is varied periodically with time, there can be a small, time-averaged resultant force which acts towards the center of the trap [25]. For a standard linear Paul trap, this is solved with dE/dx = -dE/dy, and dE/dz = 0, using the geometry shown in Figure 3-1,

3.2 The Mathieu Equation

We shall now explore how Paul traps use RF and DC potentials to spatially confine ions. This will lead us to an understanding of the behavior of the ions within the trap. Consider the rods shown in the 3D linear trap in Figure 3-1. In linear traps such as this one, the RF potential traps the ion along two dimensions, while DC trap along the third axis. The DC potential is fairly simple to understand - if positive DC voltages are applied to the ends of the rods, the ion will be trapped along that axis. However, the RF potential bears closer consideration. If an RF voltage $V = V_{RF}\cos(\Omega_{RF}t)$

is applied to a diagonal pair of rods, and the other two are grounded, the resulting potential is:

$$\Psi(x,y,z) = \frac{1}{2}V_{RF}\cos(\Omega_{RF}t)((\frac{x}{R})^2 - (\frac{z}{R})^2) \tag{3.1}$$

where R is the distance between the electrodes and the ion, as pictured in Figure 3-1.

If a DC potential is also applied to the electrodes, the resulting equations of motion are:

$$\begin{aligned} \ddot{x} &= -\frac{q_e}{mR^2}(V_{DC} + V_{RF}cos(\Omega_{RF}t))x \\ \ddot{z} &= \frac{q_e}{mR^2}(V_{DC} + V_{RF}cos(\Omega_{RF}t))z \end{aligned} \tag{3.2}$$

where q_e is the electron charge, and m is the ion's mass.

If we define the unitless parameters $a = \frac{4q_eV_{DC}}{mR^2\Omega_{RF}^2}$, $q = \frac{2q_eV_{RF}}{mR^2\Omega_{RF}^2}$, and $\zeta = \frac{\Omega_{RF}t}{2}$,these equations become:

$$\begin{aligned} \frac{d^2x}{d\zeta^2} + x(a - 2q\cos(2\zeta)) = 0 \\ \frac{d^2z}{d\zeta^2} - z(a - 2q\cos(2\zeta)) = 0 \end{aligned} \tag{3.3}$$

This is the standard form of the well-studied Mathieu differential equation [28, 30]. Solutions of this equation are said to be 'stable' when the resulting ion trajectories are bound in the trap. Different regions of stability exist in the (q, a) parameter space, but the most important one (for practical purposes) is where a $\ll 1$ and $q^2 \ll 1$. Then the ion's path has the solution:

$$x(t) = x_0\cos(\omega t_\phi)[1 + \frac{2}{2}\cos(\Omega_{RF}t)](\text{and similarly for z}) \tag{3.4}$$

where $\omega = \frac{\Omega_{RF}}{2}\sqrt{a + \frac{1}{2}q^2}$, and x_0 and ϕ depend on initial conditions.

The motion of the ion within the trap can be described with two components of the motion along each axis: a slow motion with frequency ω, called the secular frequency, and a low-amplitude fast motion at the RF frequency known as micromotion. It should be emphasized that, for linear traps such as those used in this experiment, the RF potential only traps the ion in two axes. DC potentials are applied to induce spacial confinement along the third axis.

3.3 Pseudopotential Approximation

While the Mathieu equation provides some key insights into the behavior of trapped ions, an approximation known as the 'pseudopotential approximaiton' provides a more intuitive understanding of secular motion. In the design of most traps, we can approximate a = 0, which means that the frequency of the secular motion is $\omega \approx \frac{q\Omega_{RF}}{2\sqrt{2}}$. The trap potential can be approximated as a harmonic potential that generates this secular motion along each axis. That is, the RF potential of the trap can be approximated as the 'pseudopotential':

$$\begin{aligned}\Psi(x) &= \frac{1}{2}m\omega^2x^2 \\ &= \frac{mq^2\Omega_{RF}^2x^2}{16} \\ &= \frac{q_e^2V_{RF}^2x^2}{4m\Omega_{RF}^2} \\ &= \frac{q_e^2|\mathbf{E}(x, y = 0, z = 0)|^2}{4m\Omega_{RF}^2}\end{aligned} \tag{3.5}$$

In general, the pseudopotential field can be described as a function of position $\mathbf{x}$ in an electric field $\mathbf{E(x)}$ as

$$\Psi(x) = \frac{q_e^2|\mathbf{E(r)}|^2}{4m\Omega_{RF}^2}. \tag{3.6}$$

This is very useful for simulating complex trap geometries, such as those of surface-electrode traps.

Additionally, the pseudopotential approximation makes clear the dependencies of several parameters that are important for trap design. These parameters include the trap frequencies, the stability parameter q, and the trap depth, which is the magnitude of the pseudopotential at the saddle point closest to the ion. The trap depth determines the maximum kinetic energy the ion can possess before it escapes the trap. Specifically, the trap depth $U_d \propto \frac{V_{RF}^2}{\Omega_{RF}^2 R^2}$, $q \propto \frac{V_{RF}}{\Omega_{RF}^2 R^2}$, $\omega \propto q\Omega_{RF}$ and the secular frequency along the DC-confined axis is $\omega_{DC} \propto \frac{\sqrt{V_{DC}}}{R}$. Designing the trap requires finding an RF frequency and size that satisfies the requirements for q and U_d while keeping the RF power low enough to avoid heating or damaging the trap.

3.4 Surface-Electrode Linear Paul Trap

The 3D design of original Paul traps is not very scalable. Trapping large systems of ions will require small and complicated trap architectures that would be extraordinarily difficult to machine.Fortunately, other geometries can mimic the electric field generated by a 3D Paul trap. Most notably, planar geometries can also be used to generate a field that is quadupolar near its minimum [26]. The nececary electrode geometries are discussed in more detail in [26, 31, 32]. This realization has led to the development of 2D surface electrode Paul traps, such as that shown in Figure 5-4.

A diagram of a linear SET is shown in Figure 3-2. Two parallel electrodes carry the RF voltage that creates the pseudopotential, which traps the ion along the x and z axes (as labelled in Figure 3-2). DC electrodes are used to trap the ion in the y axis. Two inner DC electrodes allow us to tilt the primary axis of the trap in the (x,z) plane. For Doppler cooling, it is crucial that there be a single beam with projections along all the primary axis of the trap. If this beam were to hit the surface of the trap, the resulting scattered light would make ion measurement difficult. The inner DC electrodes give us the control we need to avoid this problem.

Surface electrode traps (SET) can be made with standard microfabrication tech-

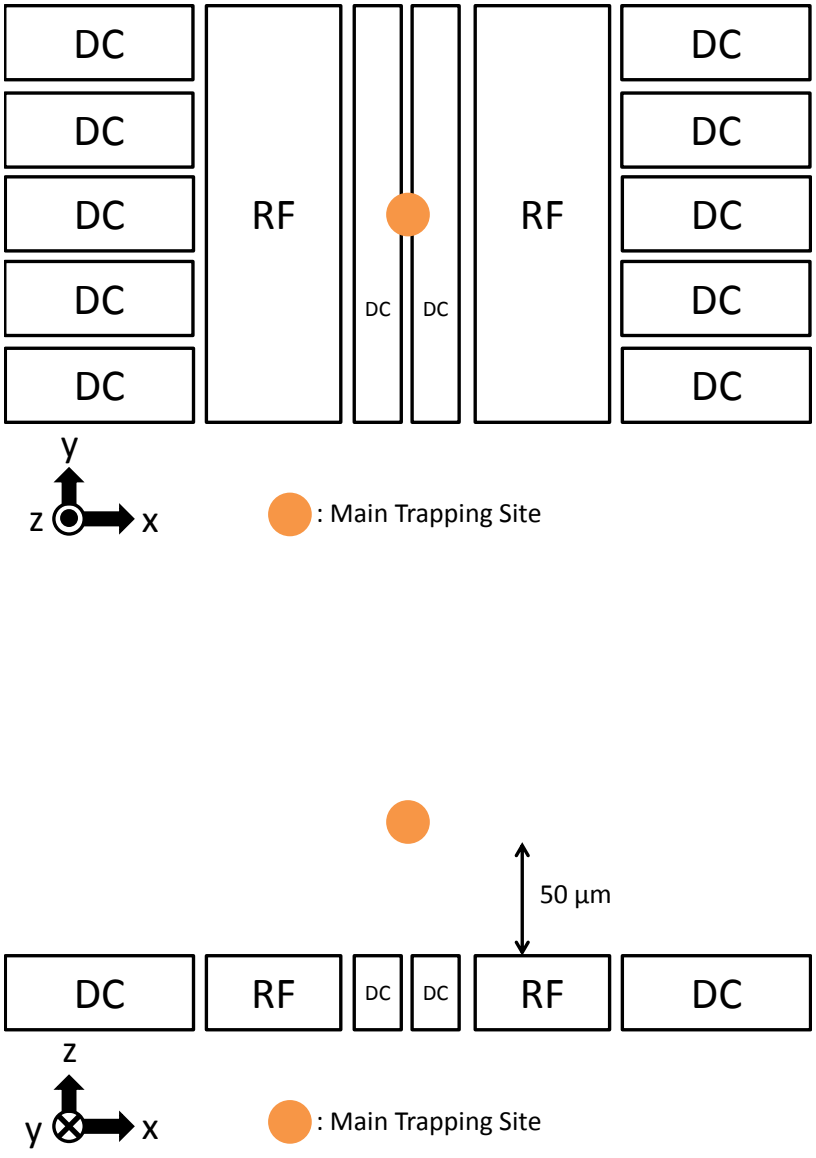

Figure 3-2: Diagrams of a linear surface electrode Paul trap from two perspectives. (top) A view from above and (bottom) a cross-section view

niques, which allows for smaller and more complicated trap architectures to be created with greater facility. Because of this, they are much more scalable than 3D traps. SETs do suffer from one great disadvantage, however. By the nature of their design, the depth of the trapping potential well generated by SETs is smaller than that of a corresponding 3D trap by a factor of 30-200 [26]. This has an adverse effect on the loading rate and lifetime of the ion within the trap. However, this difficulty is outweighed by the scalability advantages.

Chapter 4

Anomalous Heating

When there is noise in the electric field at frequency of the ion's secular motion within the trap, that noise couples to the ion's motion and increases its motional energy level. This is known as 'motional heating', and has been observed by all trapped ion experiments that have looked for it.

This motional heating presents a major obstacle to the scalability of trapped-ion quantum information processing. Two-qubit gates utilize the motional states of the ion. Even one quantum of motion absorbed from electric field noise will ruin the fidelity of this operation [33]; feasible quantum error correction demands that the average motional energy state $\bar{n}$ should not increase by more than 10^{-4} quanta during a gate operation [34, 35, 36]. Yet other sources of decoherence in two-qubit gates improve as the gate time increases. So far, the highest fidelity two-qubit gates have operation times near 100 us [6].

Furthermore, the motional heating increases rapidly as the ion's distance from the trap electrodes decreases. This distance is roughly linear with the electrode size [31]. Motional heating limits how small ion traps can be. In addition to being a scalability concern, this is again an issue for two-qubit gates, which can improve in speed as the trap size decreases.

Of course, some noise in the electric field will always be present due to thermal (Johnson) noise, blackbody radiation, etc. But the observed motional heating is several orders of magnitude larger than that predicted for common noise sources. For

this reason, it is known as an 'anomalous' heating, and has been the subject of much study. Understanding and reducing this noise would be an important step forward for trapped ion quantum information processing.

We briefly introduced this anomalous heating in the introductory chapter, but here we provide an expanded discussion. Section 4.1 provides some insight into our current understanding of this noise and its potential sources. In Section 4.2, we describe various experiments that have been able to reduce the heating rate through surface-cleaning.

4.1 Progress Towards Understanding Anomalous Heating

Several experiments have taken measurements to characterize the dependence of the anomalous heating on frequency, temperature, and the ion's distance from the electrode. Though there has been some variation in these results for frequency dependence and temperature dependence, the numbers reported here are those seen in our surface electrode trap chips. The distance-dependence measurement was taken by Deslauriers *et al.* using a 3D needle trap [9]. These results are summarized in Table 4.1, and they allow us to assess different models that predict the source of the electric field noise.

Table 4.1: Observed heating rate dependences

	Freq. Dependence	Temp. Dependence	Distance Dependence
Experimental Results	$f^{-0.6\pm0.1}$[37]	$T^{-1.59\pm.03}$ [37]	$d^{-3.5\pm0.1}$ [9]

We can begin by assessing common sources of noise. This includes blackbody radiation, noise from an external electromagnetic interference or electromagnetic pickup, Johnson (thermal) noise, and technical noise. (Here technical noise refers to equipment noise from DACs and power supplies).

The magnitude of blackbody radiation is far too low for it to be the source of the anomalous heating [38]. Technical noise would exhibit a $\frac{1}{d^2}$ distance dependence,

while electromagnetic interference or EM pick-up would not exhibit a temperature dependence. For metal trap electrodes, Johnson noise is several orders of magnitude too low to explain the anomalous heating, and it would also have a frequency dependence of $\frac{1}{f^2}$ [37]. (This changes, however, if the electrodes are covered with a thin layer dielectric, as described in the following paragraphs).

We are then forced to consider less obvious sources of noise. The experiment described in [10] found very similar heating rates for traps made with two different metals, which suggests that the noise arises from surface effects rather than from the bulk material of the electrodes. This is further confirmed by several experiments which have shown that the heating rate is reduced by surface cleaning techniques, discussed in Section 4.2. Two general theoretical models have been proposed for surface-originating noise: patch potentials and two-level fluctuators. Two physical mechanisms are also commonly discussed: adatom diffusion and dipole fluctuations. These are discussed below.

The patch potential model supposes that the electric field arises from local variations of the potential on an otherwise homogenous electrode surface. Such patches could arise from a number of factors, such as surface adsorbates or small regions of different crystal orientation. The size of these patch potentials can be determined by measuring the distance dependence of the heating rate [39]. Adatom diffusion and dipole fluctuations are commonly-discussed potential sources of patch potentials. Though neither of these models match well with our experimental results, it is possible that further refinement of the theory may lead in promising directions [37].

A recent paper about the effects of surface dielectric on Johnson noise offers another promising direction for investigation [48]. This paper predicts that very thin layers of dielectric on metal electrodes can increase thermal noise by several orders of magnitude. Such dielectrics could be adsorbates or native oxides. Assuming temperature-independent dielectric loss, the corresponding electric field noise would scale like $\dot{\bar{n}} \propto \frac{1}{d^4 f^\alpha T}$, for $\alpha = 1-2$. However, the temperature-dependence of dielectric loss varies significantly with material.

4.2 Heating Rate Reduction Through Cleaning Techniques

Several experiments have demonstrated surface cleaning techniques that cause a marked reduction in the anomalous heating rate at room temperature. The first of these was a pulsed-laser cleaning experiment which reduced the heating rate by a factor of 3 [40]. In-situ ion milling cleaning has been shown to reduce the heating rate up to a factor of 100 [1, 3, 41] This was shown to be associated with the removal of hydrocarbons from the trap surface, and for a time it seemed likely that adsorbed hydrocarbons on the trap surface were the source of a fluctuating patch potential [1].

However, a plasma cleaning experiment which also removed hydrocarbons from the trap surface only saw a factor of 4 reduction in the room temperature heating rate [2]. Furthermore, a different experiment reduced the heating rate by a factor of 10 through ex-situ milling, where the trap-chip was re-exposed to air (and thus hydrocarbons) between milling and the heating rate measurement [3]. This suggests that hydrocarbon removal does play some role in the heating rate reduction caused by ion milling, but also that it cannot fully explain the improvement seen by in-situ ion-milling experiments. Perhaps surface rearrangement from the high-energy ion-milling beams also reduces the heating rate.

Besides operation at cryogenic temperatures [9], ion-milling is the most successful technique yet discovered for reducing the anomalous heating rate. Unfortunately, it remains poorly understood.

Chapter 5

Experimental Set-Up

With the theoretical background out of the way, we can now begin to dig into the meat of this thesis: the experimental work. This chapter describes our ion-trapping apparatus, while the remaining three chapters will discuss our experimental technique and results.

Trapping ions requires several pieces of equipment. The ion must be trapped within a vacuum chamber; at atmospheric pressures there are too many particles whizzing around that would knock the ion out of the trap. In our set-up we use a cryogenic vacuum chamber, which is described in Section 5.1. To control the ion we use several different lasers, which are the subject of Section 5.2. The Paul trap itself is another important component of the experiment; Section 5.3 describes the trap chips used by our group. In Section 5.4 we describe the optical readout system used to detect and measure the ion. Section 5.5 briefly describes the electronics used to control the lasers and to deliver the appropriate voltages to the trap chip. The process of creating an ion from neutral strontium and loading it in the trap is described in Section 5.6. Lastly, Section 5.7 discusses how we minimize the micromotion of the ion to ensure that we are in a regime where the pseudopotential approximation is appropriate.

5.1 Vacuum Chamber

Ion traps must operate within an ultra-high vacuum (UHV) environment to prevent environmental particles from knocking the ion out of the trapping potential. For our system, we use a 4K cryogenic vacuum chamber, with the trap chip mounted on a temperature-controlled stage. Operating at cryogenic temperatures has two primary advantages. Material out-gassing is dramatically suppressed, allowing us to quickly reach UHV pressures after venting the chamber to atmosphere and switching traps. Furthermore, the anomalous heating experienced by trapped ion systems is greatly reduced at low temperatures. By adjusting the temperature of the trap stage, we can study the heating rate in a range of thermal conditions.

A schematic of our chamber is shown in Figure 5-1. To cool our sample mount, we use a two-stage closed-cycle Gifford McMahon cryocooler. The vibrations of the cryocooler are vigorous enough to interfere with our light-collection system, so we avoid mechanical coupling by connecting the cryocooler to the sample mount using a flexible rubber bellows. The interstitial space between the sample mount and the cold head is filled with a helium exchange gas, which forms a thermal link between the two. Windows near the trap chip allow optical access for the lasers.

The sample mount has two temperature stages. The outer stage of the mount is held at 50K, with a radiation shield that prevents thermal radiation from the chamber walls from reaching the inner 4K stage where the trap chip is mounted on a removable tower. Windows in the chamber walls and radiation shield allow optical access to the trap chip.

The tower used for mounting the trap chip is shown in Figure 5-2. It consists of a copper block with 1 mm thick alumina filter boards attached on either side. These boards have patterned gold traces. Each trace has a low-pass RC filter (R = 10 kΩ, C = 1 nF) with a cutoff frequency of about 16 kHz. An unfiltered trace is used to carry the RF signal.

At the end of the tower, a smaller copper piece referred to as the trap mount is thermally isolated from the rest of the tower with macor pieces. A small heater

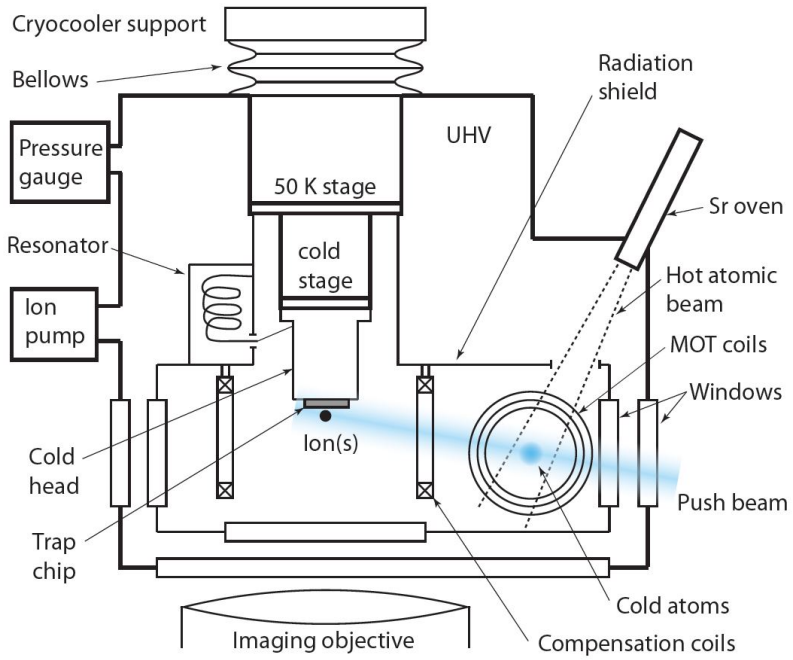

Figure 5-1: Diagram of experimental chamber for trapping ions

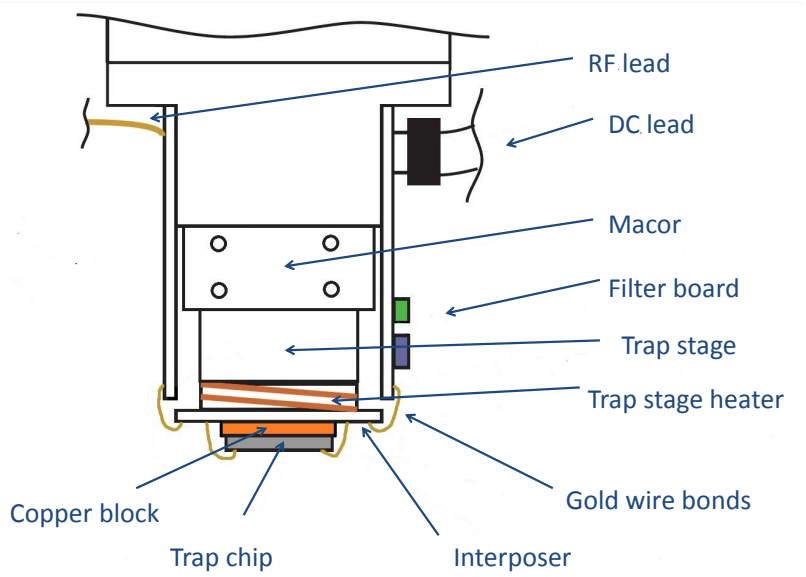

Figure 5-2: Diagram of cold head tower from ion-trapping Apparatus

at the base of the trap mount allows for temperature control. The trap chip is fixed with silver paint to a detachable copper block that screws into the bottom of the trap mount. AlN interposer pieces with gold traces are indium-soldered to the trap mount. These interposer pieces are connected with gold wire bonds to the trap electrodes and to the tower traces. A silicon-diode temperature sensor is attached to the interposer surface. When all wires are connected and the lasers are off, the trap chip reaches a temperature of 4.3K. When the lasers necessary for trapping are turned on, this temperature rises to 4.6K. The applied RF power ($\sim$ 200 mW) does not cause significant heating.

We use a turbomolecular and a 55 $\frac{l}{s}$ ion pump to reach high vacuum ($10^{-4} - 10^{-5}$ Torr) before cryocooling. UHV is primarily reached through cryocooling; we do not need to bake out the system. During standard operation we measure a pressure below 1×10^{-10} Torr; the pressure near the ion trap should be significantly lower due to more effective cryopumping.

5.2 Lasers

The 461 nm and 422 nm lasers are generated by frequency-doubling 922nm and 844 nm lasers, which produces as much as 300 mW of 461 nm and 7 mW of 422 nm. The 1092 nm is a distributed feedback laser; all others are of the external-cavity-grating stabilized design.

For laser frequency-stabilization, we stabilize the length of a Fabry-Perot 'transfer' cavity to an additional 852nm laser, which is locked to a cesium saturated absorption signal. The 922 and 844 nm and 1033 lasers are then locked to the transfer cavity using the Pound-Drever-Hall technique, giving them a $\sim$ 100 kHz linewidth. Acousto-optic modulators (AOMs) on these three lasers are used to adjust the frequency of the beams that interact with the ion to address the appropriate transitions. The 674 nm laser is locked to a Pound-Drever-Hall derived error signal from an ultrastable ULE reference cavity which is mounted vertically in a two-stage temperature-controlled vacuum system mounted on an active vibration isolation platform, resulting in a 2kHz

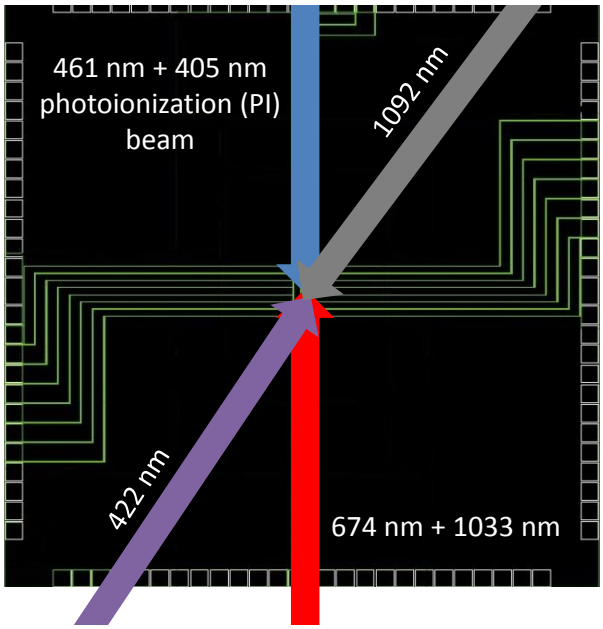

Figure 5-3: Diagram of positon of beams with respect to trap chip

linewidth. The 405nm laser is not frequency-locked, and 1092 nm laser is broadened to an approximately 0.8 GHz linewidth. This frequency broadening prevents optical pumping into dark states.

Figure 5-3 shows the angles of the beams relative to the trap chip. Near the ion, the lasers all have a beamwidth of about 50 μm. The 1092 beam is always on. The 1033 nm and 461 nm photoionization and MOT beams are switched with a TTL signal sent to the AOM driver: they can be turned on/off, but have a single power setting. AOMs do introduce loss, but shutters are too slow to control most of our lasers. Only the 405 nm photoionization beam is controlled with a shutter; it does not need to be switched quickly, and power loss in this beam is particularly undesireable because the loading rate is proportional to its power. This shutter is controlled via an SRS SR474 shutter driver. The 422 nm and 674 nm beams must both be controlled more carefully; both of these beams are used for several different purposes during the course of a measurement, and their frequency and amplitude must be adjusted by the fpga as appropriate. The AOMs for these two lasers are controlled via a WieserLabs FlexDDS multi-channel RF source. The FlexDDS stores a list of several different profiles which are loaded at the beginning of each run. The fpga then sends pulses to

the DDS to switch between these profiles as needed. Each DDS channel takes in two signals: a 'switch' signal that tells it to change profiles, and a 'direction' which tells it to either move up or down the profile list. The pattern of 422 nm pulses is simple enough that the fpga simply cycles through the list of stored DDS profiles. However, the 674 nm pulse sequence is more complicated, and the direction signal is utilized.

Each beams that is incident on the trap chip is focused with a lens mounted on a translational stage a focal length away from the trap, so that translating the lens a distance d with a micrometer moves the focus of the beam by the same distance. These stages allow us to control the alignment of the beams to the trap surface with high precision.

5.3 Trap Chip

All of the experiments described in this document were performed using linear surface electrode Paul traps with a 50 μm ion-electrode distance. Our traps are fabricated from 2 μm of sputtered niobium on a sapphire substrate. The trap chips are patterned via photolithography and dry etching with gaps of 4um between electrodes near the ions. Using sapphire as a substrate has a fortunate side-effect: the sapphire acts as a waveguide for the 422 nm laser when it is directed into the bulk of the trap chip, illuminating the gaps between electrodes. This is very helpful when aligning the lasers. An image of one of our trap chips is shown in Figure 5-4.

Figure 5-5 shows a diagram of the trap electrodes and of the entire trap chip. To ensure that the two RF electrodes are in-phase with each other, they are joined away from the trapping site. Gold pads near the edge of the trap make it easier to make gold-bond connections with electrodes. The entire trap chip is 1 cm x 1 cm. Figure 5-5 shows the bonding diagram of the trap chip, and also the labels we use for the trap electrodes. We design our traps to have $\omega_{axial} = \omega_{DC} \approx 2\pi \times 1\text{MHz}$, and the RF amplitudes we use generates frequencies along the radial, RF-confined axis of $\omega_{radial} \approx 2\pi \times 4$ MHz. For stability purposes, we design our traps to have $q < 0.4$ and we aim for a trap depth $U_d > 15$ meV. These constraints are satisfied by an RF signal

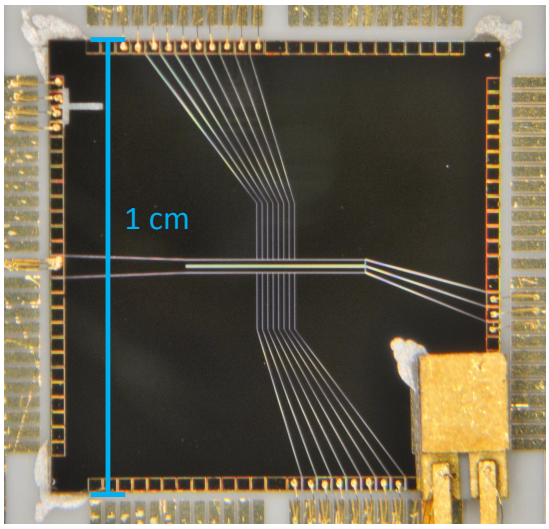

Figure 5-4: Image of linear SET trap design used by this group

Table 5.1: DC voltages used for trap chip electrodes, for axial frequencies of 0.66 MHz and 1.3 MHz. (Electrodes labelled as seen in Figure 5-5)

Axial Frequency/ Electrode	0.66 MHz	1.3 MHz
N18	-0.808 V	-1.693 V
N20	-0.218 V	-0.666 V
S6	-5.491 V	-23.594 V
N6	-6.578 V	-24.681 V
S1, S2, S3, S4	1.408 V	4.135 V
S7, S8, S9, S10	1.408 V	4.135 V
N1, N2, N3, N4	0.410 V	3.137 V
N7, N8, N9, N10	0.410 V	3.137 V

with a frequency of about 50 MHz and an amplitude near 100 V. The DC voltages we use are described in Table 5.1.

5.4 Optical Readout

Fluorescence from the ion is collected with a custom compound objective placed just outside the bottom window of the chamber, which has a numerical aperture of 0.4. The light is refocused through a relay lens onto either a photomultiplier tube (PMT) or an electron-multiplying CCD camera. The camera is used when aligning lasers and the PMT is used for data collection and micromotion detection. This system is shown

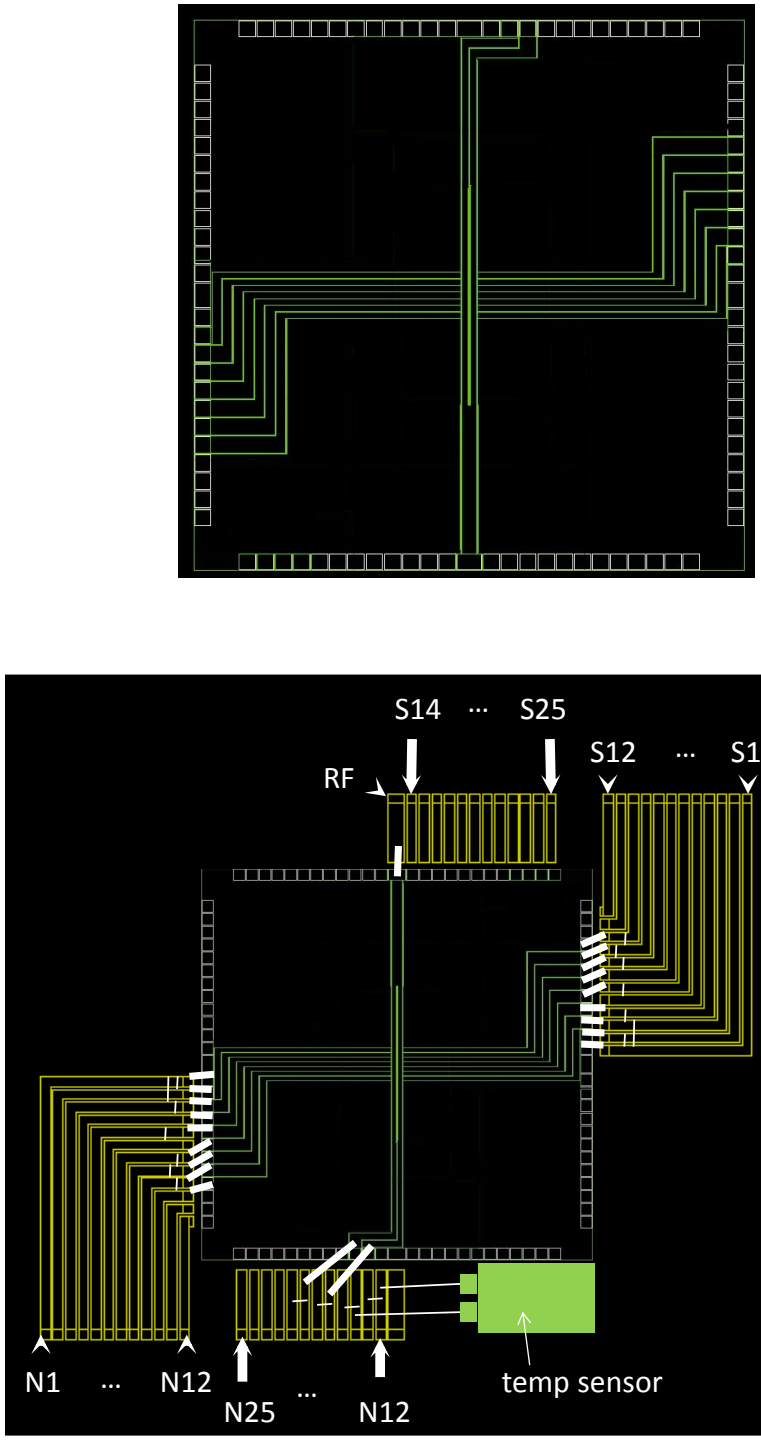

Figure 5-5: Diagrams of linear SET trap design used by this group

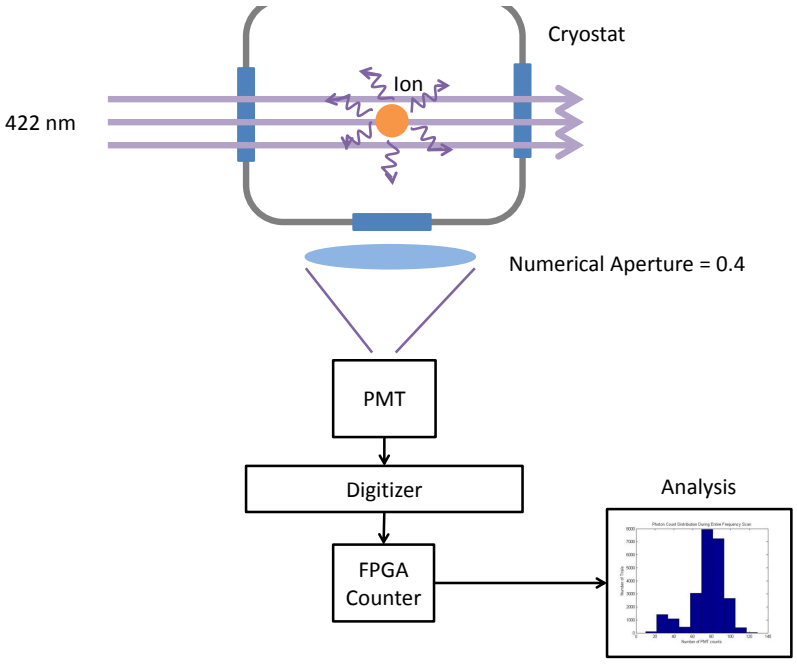

Figure 5-6: Diagram of optical readout system

in Figure 5-6. The total magnification of this system is 46x, yielding a resolution of about 1 μm when the camera is used.

Our PMT system includes an Ortec 9327 digitizer which converts the analog output of the PMT to digital pulses. The PMT has an efficiency of about 20%. During data collection, these pules are counted by the fpga. During micromotion detection, they are sent to our time-to-amplitude converter (TAC), as described in Section 5.7. Our PMT has a dark count of about 90 photons per second; our background is dominated by light scattered from the lasers off the trap chip. We use an iris centered on the ion to block most of the scatter and two filters to block light that is not from the 422 nm beam. One of the filters is a 422 nm pass filter, the other a 405 nm notch filter. Both have pass efficiencies of about 90%. We detect background scattered photons at a rate of approximately 11 kHz, and we detect fluorescence at a rate of about 23 kHz.

5.5 Electronics

The DC voltages used in our Paul trap are generated by a NI-PXI-6723 digital-to-analog converter followed by an amplifier with a voltage gain of 4.018. These output voltages are passed through a Kiwa Electronics 50 kHz low-pass multi-pole filter before being sent into the cryostat, and pass through a single-pole RC low-pass filter on the cold stage before reaching the trap chip. Typical DC voltages used for our 50 μm traps range from -24 to 3 V. Our RF voltages are generated by a SRS SG384 signal generator followed by a 29 dB amplifier. A helical resonator mounted on the 50 K stage of the sample mount is used to step up this signal to deliver the necessary voltages to the trap chip.

A National Instruments PXI-7851R fgpa is used to generate the sequence of TTL pulses to control the AOMs and shutters. This fpga also counts the digitized signals from the PMT during the measurement period.

5.6 Loading an Ion

Our experiment uses an innovative technique for loading ions. Our strontium effusion oven (typically heated to 350 C) has no line-of-sight with the trap chip, to avoid excess strontium atoms being deposited on the trap surface. Instead, the neutral strontium atoms emitted from the oven are held in a magneto-optical trap (MOT) that traps an 8 mK spherical cloud of about 10^5 neutral Sr atoms about 65 mm from the trap (see Figure 5-1). The magnetic field component of the MOT is created with coils which use 2 A of current produce a gradient of 65 G/cm in the axial direction, and the optical component is created with 60 mW of 461 nm power split into three beams with 25 mm diameters. The MOT is described in much greater detail in [42].

After the MOT is formed, we switch off the MOT beams and turn on a 461 nm push beam resonant with neutral strontium's $^1S_0 \rightarrow {}^1P_1$ transition which directs the strontium atoms towards the trap. At the trap, the 461 nm and 405 nm photoionization beams overlap with the 422 nm Doppler cooling beam (shown in Figure

5-3).

Specifically, the loading pulse sequence is as follows: the MOT beams are turned on for 40 ms. Once they are shut off, the push beam and photoionization beams are turned on for 5 ms. The 422 nm Doppler cooling beam and 1092 beam are on for the entirety of the procedure.

5.7 Measuring Micromotion

In treatment of the ion, we assume that the ion is trapped at the minimum of the pseudopotential, where micromotion is negligible. However, sometimes stray DC potentials cause the ion to be trapped away from the pseudopotential minimum. The resulting micromotion can have several adverse effects, including heating and changes in the atomic transitions [43]. When this occurs, small shifts in the DC voltages can be used to reposition the ion at the pseudopotential minimum. However, it is necessary to measure the micromotion of the ion.

To do this, we use the 'cross-correlation' technique described in [43]. Recall that the 422nm laser has a projection along all three of the primary axis of motion of the ion. As the ion motion causes it to move towards and away from the source of the 422 nm, the ion experiences a Doppler shift which brings it in and out of resonance with the 422 nm laser. The transition induced by the 422 nm causes the ion to fluoresce, and this fluorescence is much reduced off resonance. If the ion is undergoing micromotion, then its light emission will exhibit a periodic pattern at the frequency of the RF signal. It should be noted that this technique is only sensitive to micromotion along the direction of the 422 nm beam; due to the angle of our beam, we are not very sensitive to micromotion along the z-axis.

We use a time-to-analog converter (TAC) to search for any such periodicity. This device takes in two signals, a start signal and a stop signal, and it outputs an analog pulse with amplitude proportional to the time between them. We use our RF signal generator to send the TAC a 'start' pulse at the beginning of each RF period, and we use the PMT's output as the 'stop' pulse. (It is worth noting that the rate of detected

photon counts per RF period is small, as described in Section 5.4). Effectively, the TAC tracks where each photon is received relative to the RF period. The TAC pulses are passed through an analog-to-digital converter (ADC) and analyzed by our fpga, which histograms the TAC pulses based on their amplitude. This creates a plot of photon count vs. time received relative to the RF period. If this plot shows distinct trends, then there is excess micromotion. If the histogram is randomized, then the micromotion present is negligible.

Chapter 6

Heating Rate Measurement

Heating rate measurements are a key aspect of the work described in this thesis. This chapter details the methodology used to take the measurements used to compare cleaning techniques in Chapter 8.

Broadly speaking, the heating rate of an ion can be measured using the sideband thermometry technique [38]. First the ion is cooled to the ground state of its axial motion using Doppler cooling and resolved sideband cooling. After cooling ceases, the electric field noise causes the ion to heat. By measuring the average occupational level of the axial motion $\bar{n}$ after a varying time delay, the heating rate $\dot{\bar{n}}$ can be determined.

The rest of this chapter explores this measurement process in much more detail. Section 6.1 describes the pulse sequence we used in the heating rate measurements described in this work. Section 6.2 describes the alignment procedure which preceeds each measurement. Finally, Section 6.3 describes our analysis methodology for extracting the heating rate from spectroscopy data.

6.1 Pulse Sequence

As described above, the heating rate is measured by taking a series of frequency scans over the red and blue sidebands of the $^2S_{\frac{1}{2}} \rightarrow ^2D_{\frac{5}{2}}$ transition after increasing time delays. During each frequency scan, the ion is prepared to the ground state through a combination of Doppler cooling, resolved sideband cooling and optical pumping.

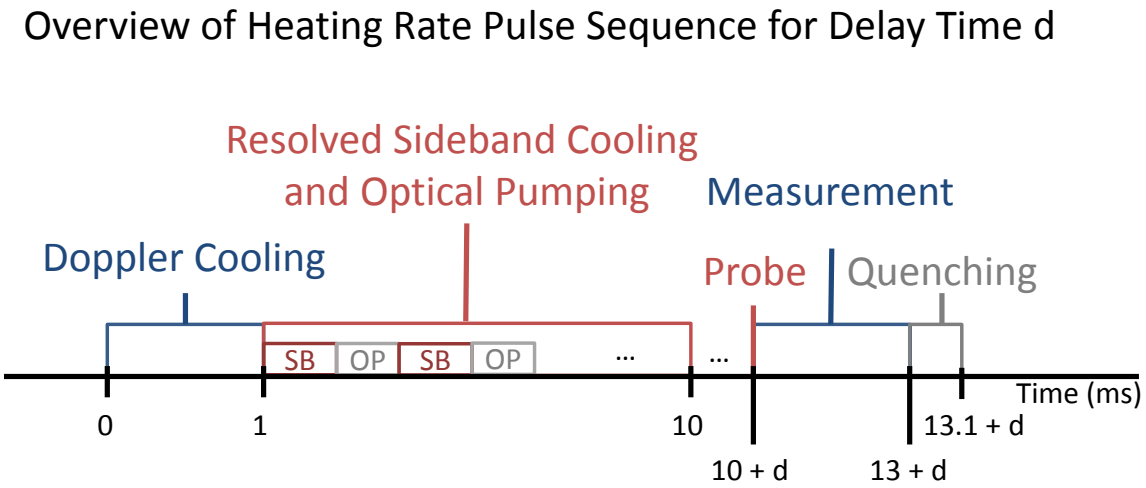

Figure 6-1: Diagram providing an overview of the pulse sequence used for heating rate measurements

After this process there is a delay period during which the ion is allowed to heat up. Once the specified delay period has elapsed the ion is treated with a probe pulse from the 674 nm laser and subsequently interrogated with 422 nm light for readout. During readout, photons seen by the PMT are counted. After the readout window has ended, the ion is quenched by the 1033 nm laser. This process is diagramed in Figure 6-1, and each part of this sequence is described in greater detail in the sections below.

This measurement process is repeated 200 times for each point in the frequency scan, and the distribution of PMT counts is used to determine the ion's distribution between the ${}^2S_{\frac{1}{2}}$ and ${}^2D_{\frac{5}{2}}$ states. During each frequency scan the frequency of the 674 nm laser is varied by 2 kHz for each point in a range of 120 kHz about the sideband transitions, for a total of 120 points in each scan.

6.1.1 Doppler Cooling

The first step in state preparation of the ion is 1 ms of Doppler cooling. During this period, the 422nm laser is on with about 15 μW of power, detuned from resonance by 20 MHz. Though the ideal detuning for Doppler cooling is $\frac{\Gamma}{2} \approx 10$ MHz, the linewidth of the transition is power-broadened. (The saturation power for the 422 nm for this transition is about 1 μW). Operating in the power-broadened regime has the advantage of making us insensitive to small fluctuations in the amplitude of the 422 nm laser.) The 1092 nm beam is on with a power of 4.6 mW, and it remains on for the duration of the experiment.

6.1.2 Sideband Cooling/Optical Pumping

During the sideband cooling and optical pumping part of state preparation, the ion alternately undergoes blocks of sideband cooling and optical pumping. The cycle of sideband cooling followed by optical pumping is repeated 20 times. A diagram of this pulse sequence is shown in Figure 6-2.

In each block of resolved sideband cooling, 674 nm pulses are alternated with quenching pulses from the 1033 nm laser. This cycle of 674 nm followed by 1033 nm is repeated 20 times. The 674 nm pulses are tuned to the red sideband of the $^2S_{\frac{1}{2},M_J=-\frac{1}{2}} \rightarrow ^2D_{\frac{5}{2},M_J=-\frac{5}{2}}$ transition. As the ion cools, the Rabi frequency of this transition decreases. We compensate for this by linearly increasing the duration of the 674 nm sideband cooling pulses. In the initial sideband cooling block, the pulses are 10 μs long. By the final sideband cooling block, the pulses are 20 μs long. We optimize the power of these pulses before each heating rate measurement to minimize the amplitude of the red sideband with zero delay (i.e., to cool the ion to the lowest temperature); typical values are 0.7 - 1.3 mW. The quenching pulses are 2 μs long, with $\sim$ 1 nW of power from the 1033 nm laser.

The optical pumping blocks also consist of alternating pulses from the 674 nm and 1033 nm lasers. Now, however, the 674 nm pulses are tuned to the $^2S_{\frac{1}{2},M_J=\frac{1}{2}} \rightarrow ^2 D_{\frac{5}{2},M_J=\frac{-3}{2}}$ transition, which is 7.34 MHz red-detuned from the carrier transition at

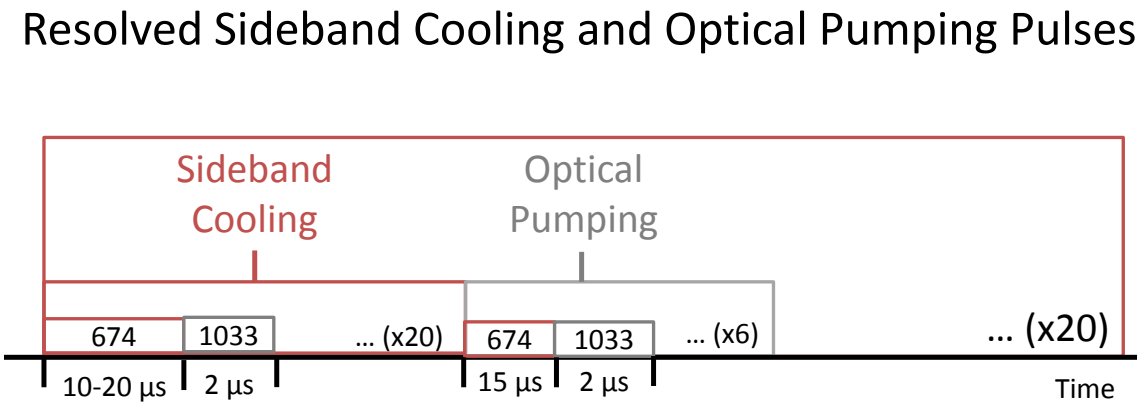

Figure 6-2: Diagram of pulse sequence for sideband cooling and optical pumping

$^2S_{\frac{1}{2},M_J=-\frac{1}{2}} \rightarrow^2 D_{\frac{5}{2},M_J=-\frac{5}{2}}$ (this detuning is B-field dependent), with a power of 2 mW. These pulses are 15 μs long, and are followed by 2 μs quenching pulses with $\sim$ 1 nW of 1033 nm power. This cycle is repeated 6 times.

6.1.3 Probe Pulse

The probe pulse from the 674 nm laser is used to send the qubit to the $^2D_{\frac{5}{2}}$ state. The subsequent measuring period detects the probability of success of this transition. As the frequency of this pulse is varied, the red and blue sidebands of the carrier transition become clear. The probe pulse is 100 μs long, with 0.4 mW of 674nm power.

6.1.4 Measurement

Directly after the probe pulse, the 422 nm laser is used to measure the state of the ion, as described in Section 2.3 and Section 5.4. During this 3 ms period, the 422 nm laser is 5 MHz red-detuned from resonance for reasons discussed in Section 2.2.1. The beam power is $\sim$ 15 μW.

6.1.5 Post-Measurement Quenching

After measurement is complete, the 1033 nm laser is turned on for 100 μs to return the ion to the ground state. The 422 nm Doppler cooling pulse is also on during this period, with the same parameters described above.

6.2 Preparing for Measurement

Before heating rate measurements are taken the lasers are carefully aligned to the ion and the relevant transition frequencies are measured. This section briefly describes our alignment process and our typical operating parameters.

Initially, the 422nm, 1092nm, and overlapped 461nm and 405 nm photoionization beams are aligned to the surface of the trap at the location where the ion will be

loaded. The CCD camera is used for this purpose. As described in Section 5.4, the input to the camera is filtered to select 422 nm light; during 422nm light is diverted as a 'tracer' and overlapped with the 1092nm and photoionization beams. Then all beams are adjusted to 50 μm off the trap surface.

After an ion is loaded, the 422nm and 1092 nm beam positions are tuned to maximize the fluorescence of the ion detected on the camera. The position of the readout objective and the readout iris are adjusted to optimize discrimination between the bright and dark states of the ion. (At this point, the ion can quickly be made dark by blocking the 1092 nm beam. Without repumping, the ion soon falls into the $^2D_{\frac{3}{2}}$ state, in which it is no longer addressed by the 422 nm light). After this process is complete, the position of the ion along the x-axis of the trap is adjusted until the micromotion is minimized, as described in Section 5.7. The position of the 674nm laser is then roughly aligned to the ion by monitoring its blinking on the camera. This blinking is caused by quantum jumps, as described in [44].

A frequency scan is used to determine the location of the $^2S_{\frac{1}{2}} \rightarrow^2 D_{\frac{5}{2}}$ carrier transition and its red and blue sidebands. The optical pumping frequency is also measured.

The alignment of the 674nm laser is improved by optimizing the Rabi frequency on the carrier transition, with 2 mW of power. Typical π-pulse times are 4-6 μs. Finally, the power of the 674 nm sideband cooling pulses is optimized by monitoring the size of the red sideband.

6.3 Data Analysis

In our experiment, raw data comes in the form of a distribution of PMT counts measured after the probe pulse at a given 674 nm frequency and with a certain delay time. This section explains how we use these PMT counts to find the heating rate. First, we use the PMT count distribution at each point in the spectroscopy to find the probability of the ion's transition to the $^2D_{\frac{5}{2}}$ state after the probe pulse. From the full frequency scan at a given delay time, we fit red and blue sidebands of the

$^2S_{\frac{1}{2}} \rightarrow ^2D_{\frac{5}{2}}$ trandition, and use the ratio of their amplitudes to measure the ion's average axial motional state, $\bar{n}$. We fit a line to the measured $\bar{n}$ after various delays, and obtain the heating rate from the slope of that fit. We shall now discuss each of these steps in greater detail.

Each frequency scan of the red and blue sidebands consists of 120 points; 60 points are taken around each sideband with a frequency step of 2 kHz. Each point represents 200 trials. The number of counts from the PMT during each trial are binned into a histogram, as shown in Figure 6-3. These counts form two Poisson distributions corresponding to the bright and dark states of the ion. The mean of these distributions varies somewhat with the surface scatter from the 422 nm, but in a measurement representative of those described in this work the dark counts had a mean centered at 35 counts and the bright counts at 86 counts. We used a threshold of 60 counts to classify measurements as either bright or dark; given the overlap in the distributions this corresponds to a miscatagorization probability of 0.002. For each point in the frequency scan, the distribution of measurements between the bright and dark states is used to find the probability p of the ion remaining in the $^2S_{\frac{1}{2}}$ state after the probe pulse. We assign an uncertainty σ_p to each of these points based on the binomial distribution: $\sigma_p = \sqrt{\frac{p(1-p)}{N}}$, where N = 200 is the number of trials.

The probability the ion making a laser-induced transition given a pulse of duration t is given by $P_{transition} = (\frac{\Omega_0}{\Omega})^2 \sin^2(\frac{\Omega t}{2})$, where Ω_0 is the Rabi frequency at resonance and $\Omega = \sqrt{\Omega_0^2 + (\omega - \omega_0)^2}$ is the generalized Rabi frequency at near-resonance frequency ω. The probability of finding the ion in the $^2S_{\frac{1}{2}}$ state after the probe pulse can be described as a function of frequency by $B - P_{transition}$, where B is some background probability of transition near the sidebands caused by primarily by carrier transitions being driven off-resonance by the 674 nm laser.

To extract the amplitude of the red and blue sidebands found from each frequency scan, we fit them both as a function of frequency f to $B - \frac{\frac{{\Omega_0}^2}{2\pi}}{\frac{{\Omega_0}^2}{2\pi} + (f - f_0)^2} \sin \pi t \sqrt{\frac{{\Omega_0}^2}{2\pi} + (f - f_0)^2}^2$, as shown in Figure 6-4. The average motional energy state $\bar{n}$ after each delay is obtained from these amplitudes as described in Section 2.3.2: $\bar{n} = \frac{r}{1-r}$. The uncertainties in the sideband amplitudes are propagated appropriately to determine the statistical

uncertainty in $\bar{n}$.

To extract the heating rate, $\bar{n}$ is determined after 5 different delay times and fitted to a line, as shown in Figure 6-5. The uncertainty in the determination of $\bar{n}$ grows as the amplitude of the red sideband approaches that of the blue sideband. For this reason, when taking measurements we try to use delay times that result in $\bar{n} < 1$, but this is often not possible for measurements taken at 295 K. Typical delay times used are 0-2 ms at room temperature and 0-40 ms at 4 K. In this work, the reported uncertainties on each heating rate measurement are statistical uncertainties obtained from the linear fit.

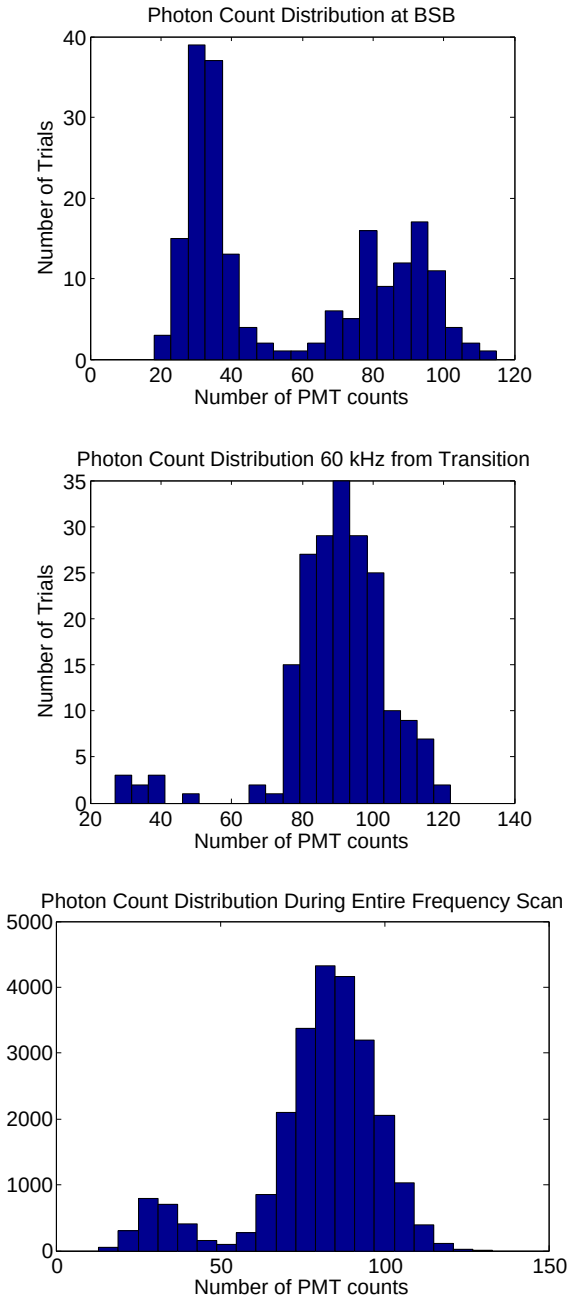

Figure 6-3: This figure contains three different plots of the PMT count distribution.The first is the distribution from a point in a frequency scan at the peak of the blue sideband, where the 'dark' distribution is clearly visibile. The second plot shows the distribution from a point in a frequency scan far from resonance (60 kHz from the carrier transition), which is more typical. The third plot combines all trials taken during a single frequency scan.

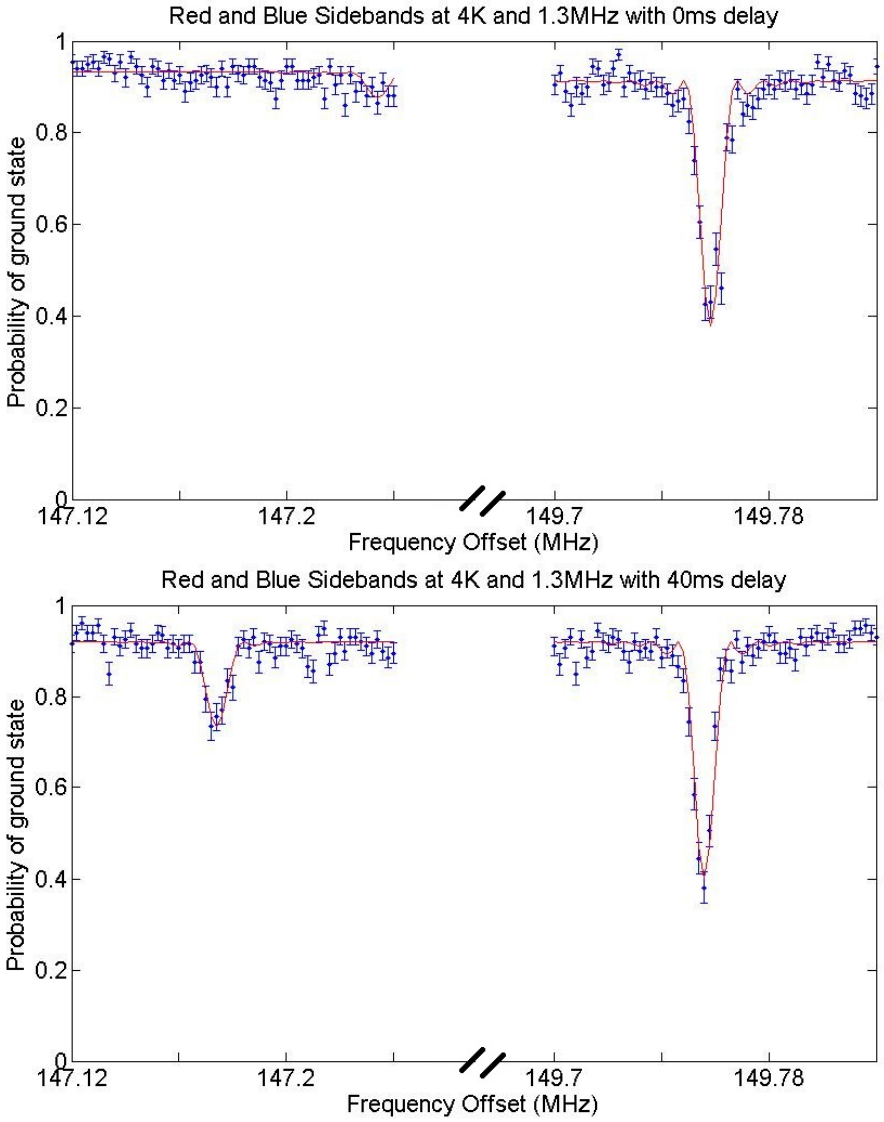

Figure 6-4: This figure displays representative fits for the red and blue sidebands of two different frequency scans. All data was taken at 4K with a trap frequency of 1.3 MHz for a standard 50 μm trap before any cleaning. The first plot shows the fits of the red and blue sidebands with a 0ms delay. The second shows the fits for the red and blue sidebands after a 40 ms delay. The heating rate fit for this data is shown in Figure 6-5.

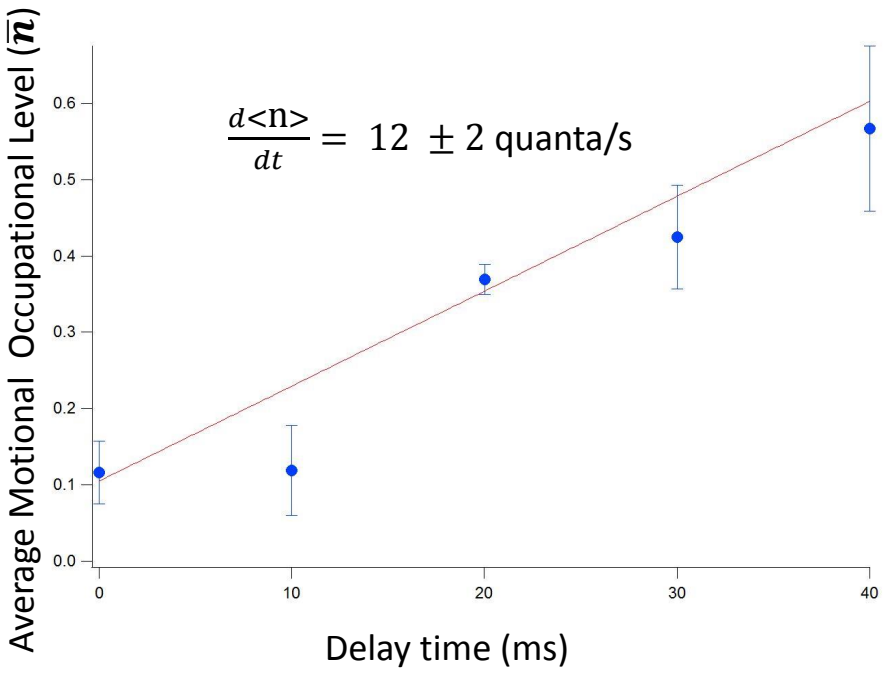

Figure 6-5: This plot shows a sample heating rate fit. All data was taken at 4K with a trap frequency of 1.3 MHz for a standard 50 μm trap. The fits for the red and blue sidebands from the 10ms and 80ms points are shown in Figure 6-4.

Chapter 7

Designing a More Scalable Resonator for RF Delivery

As trapped ion systems move towards scalability, the accompanying electronics must also be scalable. Large, complex trap architectures will likely need many parallelizable signal sources. Concretely, this means the electronics must be small, power-efficient and easily assembled. One particular component that lacks these properties is the helical resonator commonly used to deliver a high RF voltage to the trap chip. To limit capacitive losses and RF cross-talk in the long cables to the cryostat, a low-voltage RF signal is sent into the chamber and then amplified with a passive resonator to the higher voltages required to generate the trapping potential. Historically, this has been accomplished with helical resonators [45].

Helical resonators are similar in principle to quarter-wavelength coaxial resonators. They operate through inductive coupling and can be described in terms of their distributed inductance, capacitance and resistance. The Q of a helical resonator depends strongly on the thickness of the wire used to wind its inductive coils, and on the ratio of the coil diameter to the wire thickness. These resonators are described in further detail in [45].

Helical resonators suffer from two key limitations. The first is one of size. It is difficult to make these resonators small, so making an array of resonators is impractical for large trap arrays. These resonators are also challenging to design and build, with

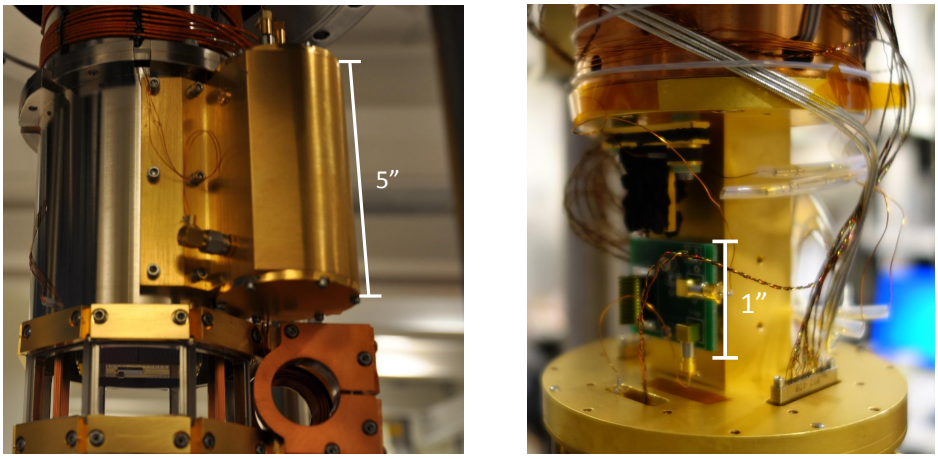

Figure 7-1: This figure pictures (left) the helical resonator formerly used by our experiment, in contrast with the new resonator board (right).

stray capacitances that are difficult to model and parts that must be custom-made. Changing the RF frequency by more than a few MHz requires carefully winding a new coil by hand.

In this chapter we present a more scalable alternative to the helical resonator. Inspired by [46], we designed a small resonator board made entirely from off-the-shelf components which fits on a 1 inch by 1 inch PCB board and delivers an 52 MHz signal with an amplitude of $96 \pm 1 V_{RF}$ to the trap chip using 74 mW of power (corresponding to a Q of 200). In contrast, the helical resonator formerly used in our lab was 5 inches high with a 2 inch diameter and only had a Q of 90. Figure 7-1 compares the new resonator board to the helical resonator. Section 7.1 discusses the theory behind the design of the resonator circuit, while Section 7.2 describes the experimental implementation of the board, including the components used and our results upon testing it within our system. Finally, Section 7.3 contains our conclusions and outlook.

7.1 Design

This resonator board was designed with two primary concerns: small size and low power consumption. The circuit used for the resonator board can be broken up into

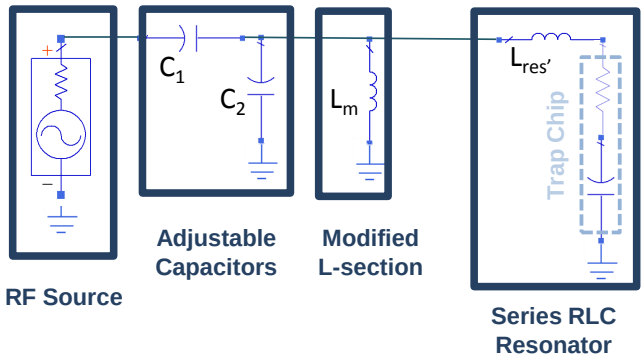

Figure 7-2: Circuit diagram for resonator board

two key sections: the series RLC resonator, where the voltage step-up occurs, and the matching network which maximizes the power delivered to the resonator. The design of both sections is discussed below. A schematic of the complete circuit is shown in Figure 7-2.

7.1.1 RLC Resonator

A series RLC resonator serves as the critical part of the circuit where the voltage gain occurs. We selected this type of resonator because it can offer a large voltage gain with small, easily-assembled components. A canonical RLC resonator has three physical components: the eponymous resistor, inductor and capacitor. However, in our design the resistance comes only from the effective resistance of the circuit. The circuit's capacitor comes from the capacitance of RF electrodes of the trap chip to ground as well as any stray capacitance to ground from the wiring which connects the circuit to the trap chip.

On resonance, the voltage gain of an ideal series RLC resonator is equal to its quality factor Q, where $Q = \frac{1}{R}\sqrt{(\frac{L}{C})}$ and the resonant frequency $\omega_0 = \frac{1}{\sqrt{LC}}$. This can be seen by treating the series RLC circuit as an impedence divider:

$$\begin{aligned}\frac{V_{capacitor}}{V_{in}} &= \frac{\frac{-i}{\omega C}}{R + i\omega L + \frac{-i}{\omega C}} \\ &= \frac{-i}{\omega C(R + i(\omega L - \frac{1}{\omega C}))} \\ &= \frac{-i}{\omega CR} \text{on resonance} \\ &= \frac{-i}{R}\sqrt{\frac{L}{C}}\end{aligned} \tag{7.1}$$

To maximize the gain, R and C must be minimized for the desired resonant frequency.

Trap chips have range of capacitances depending on their design - multilayer traps have a higher capacitance, for example. The board described in this work was designed to be used with a trap chip that has a 22pF capacitance when connected to the tower of our system. For our traps, the tradeoff between the trap depth and stability parameter q (described in Section 3.3) is well satisfied for RF frequencies around 50 MHz. When considering appropriate inductors, we selected for small commercial components with a low effective resistance. The effective resistance of the circuit decreases even further at the cryogenic temperatures within our system, increasing the gain.

7.1.2 Matching Network

The power delivery of an RF circuit is maximized when the impedance of the system is matched, i.e., when the load has the same impedance as the source. Typical RF sources have a 50 Ω impedance. However, the on-resonance impedance of the RLC resonator is simply the circuit's resistance, which we designed to be much smaller than 50 Ω. To maximize the voltage delivered to the trap chip we need a matching network to increase the impedance of the load. This transformation of impedance leads to a corresponding drop in voltage over the matching network (discussed more in the next section). However, the reduction in reflected power more than makes up for this. Additionally, for our application it is important to avoid DC bias on the RF

signal, since such a bias would perturb the trapping potential. To avoid this bias, we want there to be a DC path from the trap chip to ground. With these considerations in mind, our matching network was based on the simple 'L-section' design.

L-sections are comprised of two passive components, one connected in series and the other to ground. By adding impedances in this way, the effective load impedance can be altered as desired. A typical high-pass L-section which increases the load impedance has a shunt inductor and a capacitor in series with the load, as pictured in Figure 7-3. This arrangement does not have a DC path to ground if lumped components are used; it is undesirable to have a matching capacitor in series with the trap chip. At first glance, this seems to mean that some other matching network design must be used.

However, upon closer consideration we find that a small modification to the standard L-section will serve our purposes quite nicely. The physical components within the L-section are not as important as the impedances they provide. Adding a capacitor in series with the L_{res} inductor is one way to make the desired impedance change, but instead of having a capacitor and an inductor with a summed impedance of $i\omega L_{res} - \frac{i}{\omega C_{matching}}$, we can replace both components with single inductor $L_{res'}$ that will have the same impedance on resonance: $L_{res'} = L_{res} - \frac{1}{\omega_0^2 C_{matching}}$. This modification will result in the same impedance on resonance, but it leaves the trap chip with a DC path to ground. This substitution is visualized in Figure 7-3.

In general, the component values for the matching network are chosen based on the load impedance. This presented a difficulty, as the resonant load impedance of the RLC circuit is the effective resistance of the system, which is temperature dependent and difficult to determine precisely. Based on previous measurements, we estimated the approximate resistance of the system to be 1 Ω. To allow some additional flexibility in the impedance matching, however, we added two additional capacitors before the matching circuit. Unlike inductors, high-Q commercial capacitors have a standardized size and have finely-spaced available values. We hoped to use these extra capacitors to tune the matching once the resonator board was assembled. Though they served this purpose to some extent, we ultimately adjusted the

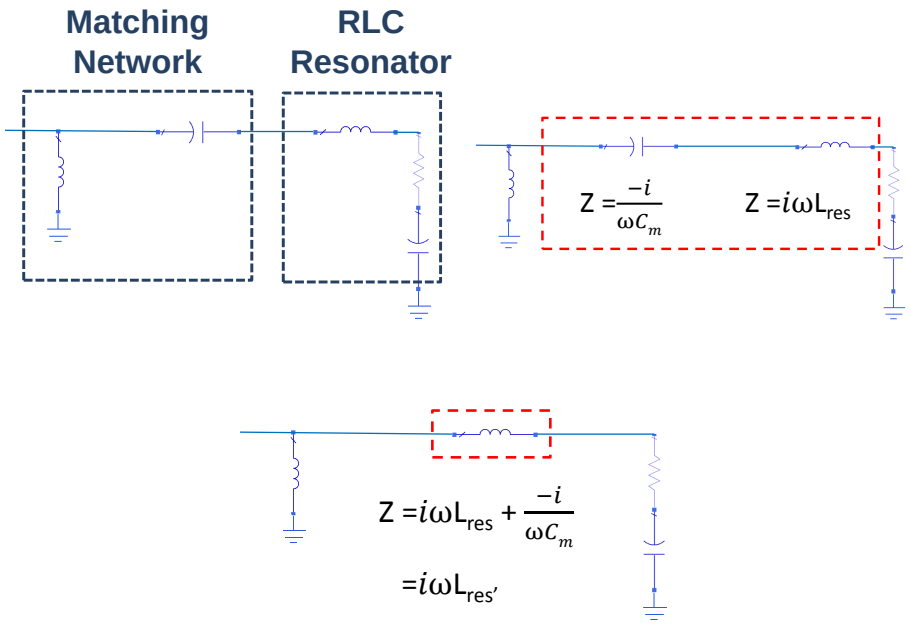

Figure 7-3: This figure depicts the matching network used in the resonator board. (top right) shows the typical L-section matching network used for high-pass systems with load resistance less than the source resistance. (top left) shows the impedence of the matching capacitor and resonant inductor. In the resonator board, these two components are substituted with one with an equivalent impedance on resonance, as shown in (bottom).

impedance matching by adding lengths of cable to the transmission line that delivered RF into the cryostat. These cables have a capacitance of about 100 $\frac{pF}{m}$. Given the $\sim$0.3 m of cable used, our impedance-matching was off by a few tens of pF.

While an impedence-matched resonator does deliver a higher voltage than one that is unmatched, matching networks do reduce the ideal resonator gain. Matching networks are akin to transformers - they contain non-resistive elements, so they conserve power, but the change in impedance leads to a change in voltage. Since our matching network transforms from a high impedance to a low impedance, it also decreases the voltage amplitude of the signal, as shown below:

$$\begin{aligned} P_{in} &= P_{out} \\ \frac{V_{in}^2}{Z_{in}} &= \frac{V_{out}^2}{Z_{out}} \\ \frac{V_{out}}{V_{in}} &= \sqrt{\frac{Z_{out}}{Z_{in}}} \end{aligned} \tag{7.2}$$

Here, $Z_{in} = 50\ \Omega$, and on resonance $Z_{out} = R_{resonator} = \frac{1}{Q}\sqrt{\frac{L}{C}}$

7.1.3 Calculating Gain

The ampltidue of the voltage at the trap, V_{trap}, can be calculated as a function of easily-measured paramaters of the circuit. We begin with an expression for the total voltage gain, which is the product of the voltage loss over the matching network and the step-up from the resonator.

$$\frac{V_{trap}}{V_{in}} = \sqrt{\frac{Z_{out}}{Z_{in}}} Q_{resonator} = \sqrt{\frac{\omega_0 L Q_{resonator}}{Z_{in}}} \tag{7.3}$$

By substituting in $P_{in} = \frac{\langle V_{in}\rangle^2}{Z_{in}} = \frac{V_{in}^2}{2Z_{in}}$, (where V_{in} is the amplitude of the input voltage and $\sqrt{\langle V_{in}^2\rangle}$ is the root mean square) we find:

$$fV_{trap} = \sqrt{\frac{\omega_0 L Q_{resonator}}{Z_{in}}}\sqrt{\frac{P_{in}}{Z_{in}}} = \sqrt{2\omega_0 L Q_{resonator} P_{in}} \tag{7.4}$$

The loaded Q of the system can be measured from the S11 parameter: $Q_L = \frac{\omega_0}{\delta\omega}$, where $\delta\omega$ is the -3dB full-width bandwidth of S_{11}. The loaded Q incorporates the internal Q of the load (Q_I) and the external Q of the RF source (Q_E): $\frac{1}{Q_L} = \frac{1}{Q_E} + \frac{1}{Q_I}$. When impedances are matched, $Q_E = Q_I$, and $Q_L = \frac{1}{2}Q_I$. Here, Q_I is $Q_{\text{resonator}}$.

$$V_{\text{trap}} = 2\sqrt{Q_L L \omega_0 P_{in}} \tag{7.5}$$

7.2 Experimental Realization

Using the design principles described in the previous section, we built a resonator circuit with a simple custom PCB board desing and several off-the-shelf components. This section begins with description of the physical board, and then moves to a discussion of the results obtained from testing the board in a liquid He dewar and then in our ion-trapping apparatus, where it was sucessfully used to trap ions.

7.2.1 Board Layout and Components

The board design is shown in Figure 7-4 It is implemented on double-sided PCB made from 0.062 inch FR-4 epoxy glass with a copper thickness of 0.0017 inches. Two though-holes allow it to be easily mounted to the tower inside our cryochamber.

The need for small, high-Q and temperature-stable components led us to use air core inductors from Coilcraft and NP0 ceramic capacitors from Capax. A list of the components used and their values is shown in Figure 7.1. Except for the PCB board, all of the nececary parts are low-cost, off-the-shelf components. The board itself is a straight-forward design that is easy to reproduce.

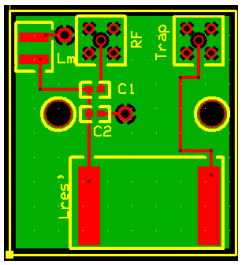

Figure 7-4: Layout of the resonator board on PCB.

RF	GPPO connector
C_1	100 pF
C_2	18 pF
L_m	27 nH
$L_{res'}$	430 nH
TRAP	GPPO connector

Table 7.1: Components used in resonator board

7.2.2 Ex-situ Testing

After the board was assembled, preliminary tests at 4K were conducted inside a liquid helium dewar with a 22pF capacitor replacing the trap chip. The set-up for these tests is shown in Figure 7-5.

At room temperature, the resonator had a Q of 55, a resonant frequency of 43.6 MHz and the quality of the impedance matching was -25.7 dB. When the board was immersed in the dewar, it had a Q of 170, a resonant frequency of 44.66 MHz and the quality of the impedance matching was -18 dB.

7.2.3 Trapping an Ion

The resonator board was mounted to the tower of one of our cryogenic ion-trapping systems and connected to the trap chip. The circuit was tested at room temperature, and at 4K and was then used to trap ions.

The S_{11} plots at room temperature and 4 K are shown in Figure 7-6. When warm, the resonator had a Q of 65, a resonant frequency of 50.67 MHz and the quality of the impedance matching was -6 dB. Once the system was cooled to 4 K,

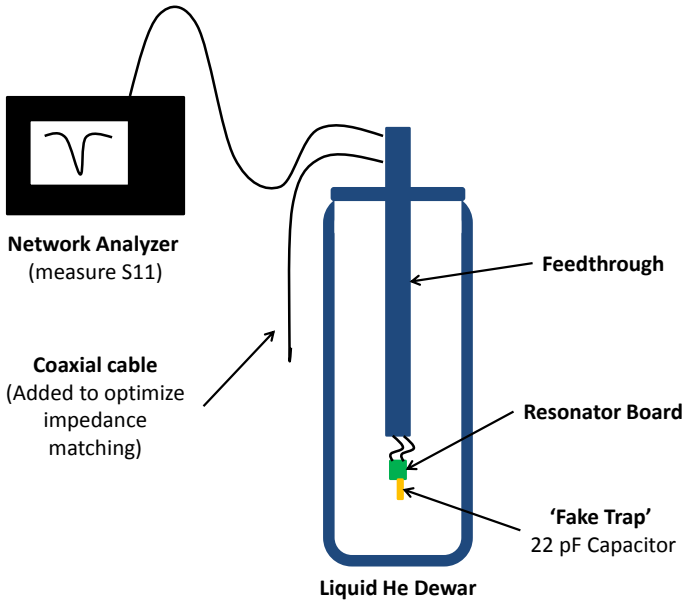

Figure 7-5: Set-up for initial testing of resonator board in a liquid helium dewar.

the resonator had a Q of 201, a resonant frequency of 52.28 MHz and the quality of the impedance matching was -16.3 dB. Though the resistivity of pure copper changes by 800% between 295K and 4K [47], we would not expect the resonator Q to change by such a large factor due to impurities in the copper used for the traces and the solder used to attach components. Based on the expression derived in Section 7.1.3, this Q corresponds to a voltage with amplitude of 91 V_{RF}.

After these measurements were taken, the resonator board was used to successfully trap ions. The input RF signal was 18.7 dBm, or 74 mW. We then measured the secular frequencies of the ion along the three primary axis of the trap. As described in Section 3.3, the radial secular frequencies of the ion's motion are a function of the amplitude of the RF signal. Given these frequencies, we can determine V_{RF} by varying the RF amplitude in a simulation of the trap chip until the simulated frequencies match the measured ones.

The secular frequencies along the radial axis of the ion can be measured by adding a small RF signal to an electrode that generates an electric field at the ion's position with some component along the relevant axis. When the RF signal is resonant with

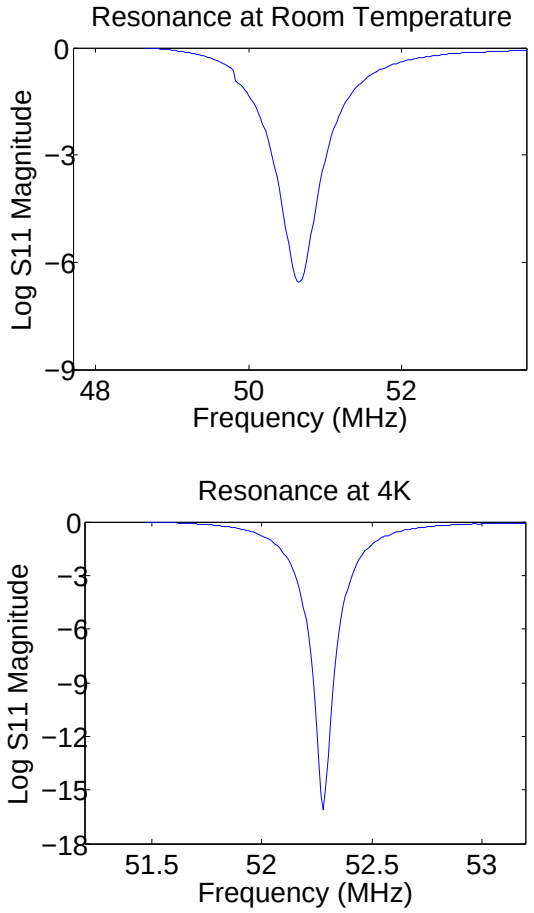

Figure 7-6: This figure shows the S_{11} measurements taken of the resonator board when it was mounted in our ion-trapping system. These were used to extract the Q values of the resonator. (left) Shows the impedance matching at room temperature, and (right) at 4K.

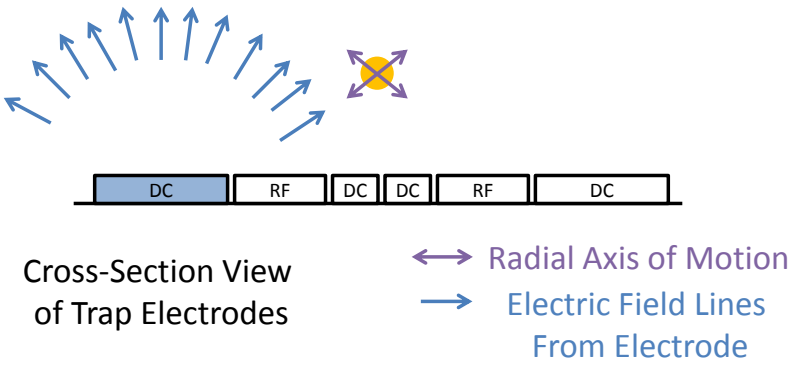

Figure 7-7: Visualization of the electric field lines from the DC electrode used for tickling and the axis of the ion's radial motion

the secular frequency along that axis, it couples to the ion's motion. The resolution of our CCD camera is fine enough that this motion can be detected; the ion's flouresence becomes spacially smeared along the axis and the ion appears 'fuzzy' on the screen. The secular frequency can be determined by varying the frequency of the additional RF signal until this 'fuzziness' is observed. This process is sometimes known as 'tickling' the ion. The coupling of the RF signal to the ion's motion depends on the dot product of the electric field lines seen by the ion with the axis of motion (visualized in Figure 7-7), so we used DC electrode N10 for tickling. To generate the desired signal, we disconnect the desired DC electrode from the usual electronics and instead connect it to a signal generator capable of producing an AC signal with a DC offset. The DC offset is set to the usual voltage of the electrode. The amplitude of the RF signal used was 1 V AC; the various filters on the sample mount reduce this to about 1 μV at the trap chip. The radial secular frequencies measured with this process were 4.1 MHz and 4.69 MHz. In simulation, this coresponds to an RF signal at the trap with amplitude $96 \pm 1 V_{RF}$. This agrees well with the calculated value of 91 V_{RF}.

7.3 Summary and Outlook

In summary, we have designed a resonator board to replace the helical resonator used in ion trapping systems. The chief contribution of this new design is that it consists entirely of off-the-shelf components. The new resonator board is more compact, easier to assemble and has a substantially higher Q than the helical resonator. This represents a small but useful step towards a more scalable experimental set-up. Currently, these boards are used in two of our group's ion trapping chambers. It seems likely that the dramatic improvement in the Q value was primarily achieved because the new resonator board was small enough to fit on the 4 K stage of the sample mount, where the helical resonator had to sit on the 50 K stage.

However, there is still room for improvement. Our method of manually adjusting the impedance matching by attaching additional lengths of coaxial cable would be

inconvenient and unwieldy for larger architectures that use multiple RF sources. In the future, external tunable capacitors would provide a better technique for optimizing impedance matching. Variable capacitors with impedances in the same range as that of the added cables can be also be purchased off-the-shelf.

Chapter 8

Ex-Situ Ion Milling with Plasma Cleaning

As discussed in Section 4, the ion milling experiment described in [1] is one of the primary pieces of evidence pointing towards the anomalous heating arising from surface effects of the trap chip. In this experiment, the NIST ion trapping group was able to achieve a hundred-fold reduction in the heating rate of a gold trap chip through ion milling, and this improvement was correlated with the removal of hydrocarbons from the trap surface, as measured with Auger electron spectroscopy (AES). However, in-situ ion-milling is not an ideal cleaning technique: the high-energy ion beams can cause undesired resputtering of metal from the trap electrodes [2], and it is difficut to incorporate the required hardware in many systems.

Recently, our group implemented a gentler alternative cleaning method, in the form of in-situ plasma cleaning, which was tested on a Nb trap [2]. Plasma cleaning also removed hydrocarbons, but ions in an RF plasma have much lower energy than those used in the ion-milling experiment (on the order of eV versus keV). However, while plasma cleaning did improve the heating rate by a factor of four, it did not obtain the anticipated degree of improvement through hydrocarbon removal.

Ex-situ milling experiments performed by the NIST group suggested that the heating rate reduction from ion-milling might not come solely from hydrocarbon removal [3], but perhaps also from a restructuring of the trap surface. To investigate

that possibility, we have designed an experiment where the trap chip is first cleaned through an ex-situ ion-milling process and then through an in-situ plasma cleaning. The initial ion-milling would both remove hydrocarbons and induce any concurrent surface re-structuring. The hydrocarbons would be reintroduced when the trap was moved from the ion-milling chamber to the ion-trapping apparatus, but it would be removed again upon plasma cleaning. If ex-situ ion-milling followed by in-situ plasma cleaning showed an improvement over plasma-cleaning alone, this would point to surface restructuring being a key mechanism of the heating rate reduction caused by ion-milling.

To investigate this possibility, we compare the heating rates of a single trap chip before cleaning, after ex-situ milling, and after ex-situ milling and plasma cleaning with previous results from a plasma-cleaned trap chip of the same make. Section 8.1 describes the ex-situ milling chamber used for this experiment. Section 8.2 describes our experimental procedure and results, and Section 8.3 provides a conclusion and outlook.

8.1 Ex-Situ Milling Chamber

Our ex-situ ion milling chamber was designed to reproduce ion milling conditions similar to that described in [1], where the NIST group reduced the heating rate by a factor of 100. We begin by describing the chamber design, and then we describe a preliminary test that demonstrated the functionality of the apparatus.

8.1.1 Chamber Design

A diagram of our ex-situ ion milling chamber is shown in Figure 8-1. At one end of the chamber, the trap chip to be milled is mounted on a tower like that described in Section 5.1. The electrodes of the trap chip are individually connected via gold wire bonds to lines running down the tower, and two PEEK (polyetheretherketone) connectors with ultra-lightweight XLETFE wire connect the tower to two 25-pin sub-D feedthroughs. Outside the chamber, the connections to the electrodes are joined

in two groups corresponding to the 'north' and 'south' halves to the trap chip. By separately measuring the current on these two groups we were able to determine when the ion beam was centered on the trap chip, as well the net rate of incident ions. High vacuum is achieved with two turbomolecular pumps; a second pump is used after the 6"-2.5" reducer because the ion gun filament will burn out at pressures above 1×10^{-5} Torr, and there is poor conductance across the shutter.

Our ion sputtering gun is a Model IPS3-D produced by Vacuum Microengineering Inc. This gun consists of a filament ion source with external permanent magnets and electrostatic lenses. When a few-amp current is run through the filament, ions are produced from inert gas atoms in the cell via electron impact ionization in the magnetic field. A positive potential accelerates the ions through the cylindrical tube of the ion gun. The ion sputtering gun is positioned such that the incident beam of ions is perpendicular to the trap surface.

After a bakeout at 130 C, our chamber was able to reach pressures of 9×10^{-7} mbar.

8.1.2 Preliminary Testing

As a preliminary test of the ex-situ milling chamber, we milled a previously-measured 40nm-thick gold-film trap. The initial pressure of the chamber was 9×10^{-7} mbar, which increased to 1.4×10^{-6} mbar after the filament current was turned on and before the Ar was introduced. We milled the chip for one hour with a filament current of 2.72 A (corresponding to an emission current of 30 mA), a total pressure of 7.2×10^{-6} mbar (5.8×10^{-6} mbar of Ar) and a 2 kV acceleration voltage. During this time, the trap current ranged from 1.05 μA to 1.2 μA, with about 0.53 μA and 0.65 μA from the north and south sides of the trap, respectively.

After milling, the surface of the trap showed a clearly visible, roughly circular transparent region with lighter regions around the edges. This is shown in Figure 8-2. Under the microscope, a second image of the trap electrode pattern can be seen in the dark region, which is the reflection of the electrode pattern off the surface below the substrate. The skin depth of Au at visible wavelengths is on the order of

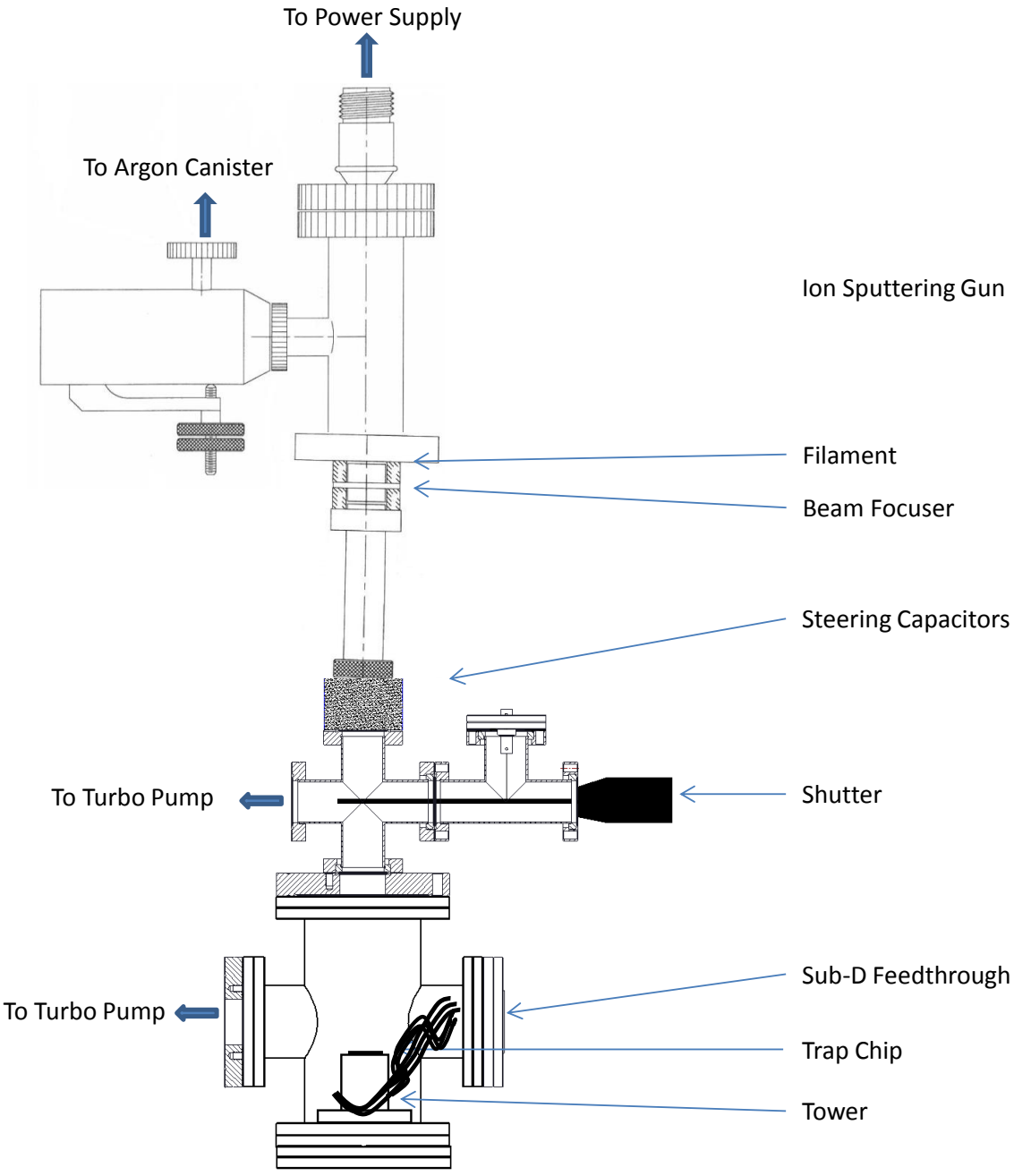

Figure 8-1: Setup for ex-situ ion milling.

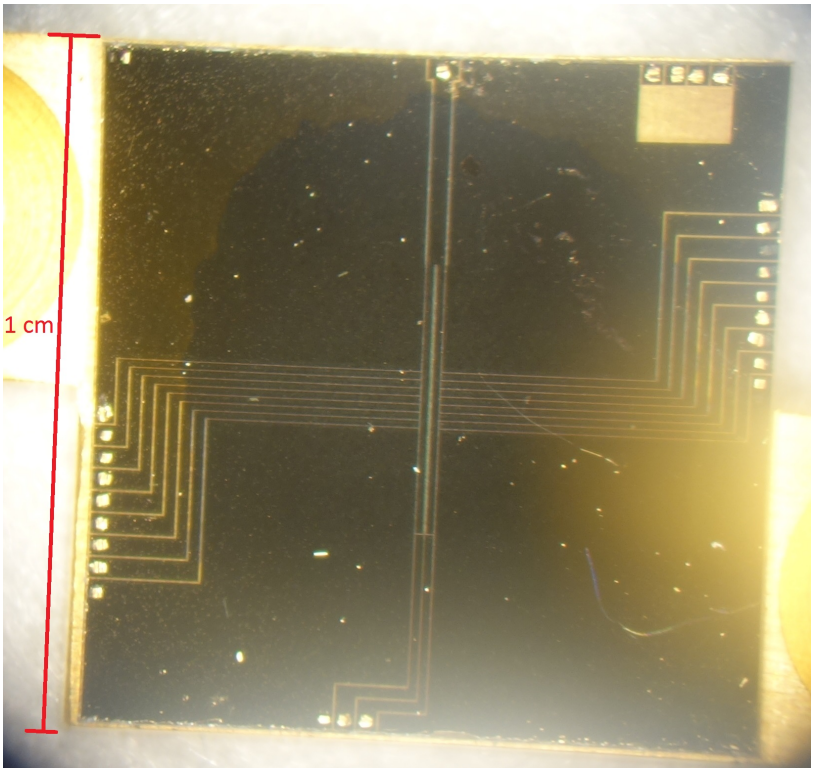

Figure 8-2: This figure contains an image of a 40nm thick gold trap after it was milled for an hour. The transparent patch in the center of the trap chip is an area where 10-20 nm of gold was removed by milling; this indicates that ion milling was successful.

10nm, so this indicates that the ion milling was successful and removed 10-20nm of gold from the dark region of the trap.

8.2 Experimental Implementation

We chose for this experiment a 50 μm trap chip made of 2um of sputtered Nb on sapphire. This trap chip was chosen to have the same design and material as that used in the previous plasma cleaning experiment [2], to allow for a better comparison of heating rate reduction. We began by taking several pre-cleaning heating rate measurements at room temperature and at 4K, for axial trap frequencies of 0.66 MHz and 1.3 MHz.

We then milled the trap for one hour with a 2 kV acceleration voltage and a total pressure of 7.0×10^{-6} mbar (5.5×10^{-6} mbar Ar). We optimized the beam steering

until we saw a trap current of 1.3 μA, with 0.66 μA and 0.61 μA from the 'north' and 'south' halves, respectively. At this point, the integrated ion-flux density was $\sim$48 $\frac{C}{m^2}$. After milling, we re-measured the heating rates.

We next performed in-situ plasma cleaning for 75 minutes, which was the duration at which the cleaning effect saturated in [2]. For this procedure, we use a gas mixture of 50 % Ar, 30% N_2 and 20% O_2, with 800 mtorr total system pressure and 15 W of RF power. After plasma cleaning, we again measured the heating rates.

Figure 8-3 shows the results of these heating rate measurements. For the sake of comparison, these plots include the heating rates of a similar trap measured after plasma cleaning (with no ion milling) by our group in the experiment described in [2]. It is clear in that the ex-situ milling and plasma cleaning did not offer an improvement over plasma cleaning alone.

To ensure that our ion milling was comparable to that described in [1], we milled the same trap again to increase the total integrated ion-flux density. (The integrated ion-flux density reported in [1] was $90\pm20\frac{C}{m^2}$). During this second milling the chamber pressure and acceleration voltage were the same as in the first milling, described above. This time, we split the connections to the trap electrodes into four groups, so as to measure the current coming from four quadrants of the trap chip. The total current was 1.4 μA, with 0.3, 0.4, 0.3 and 0.4 μA seen from each quadrant, confirming that the beam was centered on the trap chip. We milled for two hours, resulting in an integrated ion-flux density of $\sim$100 $\frac{C}{m^2}$ from the second milling. We again took heating rate measurements with the trap chip at 4K and 295K, with a trap frequency of 1.3 MHz. Following this second milling, we again plasma cleaned the trap chip, with the same parameters described above. After plasma cleaning, we took more heating rate measurements. Our results from this second round of milling are shown in Figure 8-4.

For the measurements taken at room temperature, it is clear the additional ex-situ milling offered no improvement in the heating rate. The initial heating rate measurements from this experiment and from [2] are within uncertainty of each other, as are the final heating rates after plasma cleaning.

The case is slightly less obvious for the measurements taken at 4K; the compari-

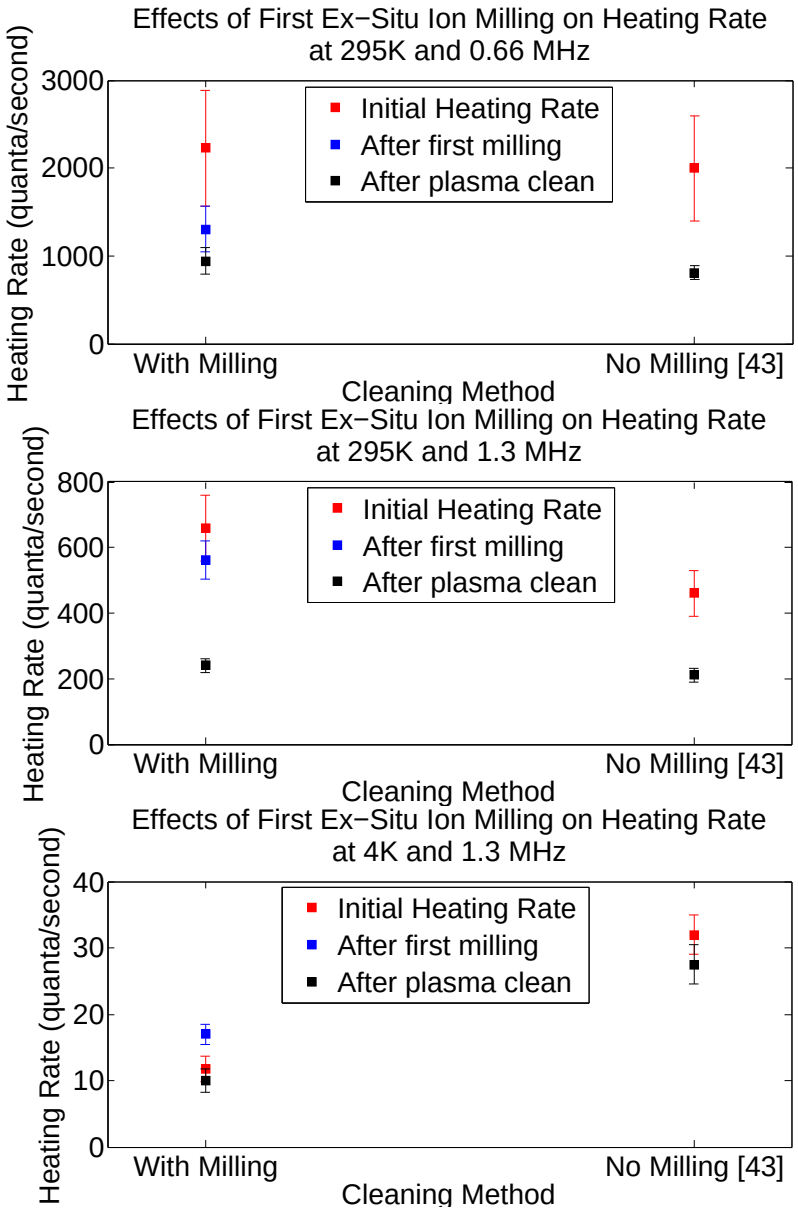

Figure 8-3: This figure compares heating rate reduction after cleaning via ex-situ ion milling and plasma cleaning with reduction after plasma cleaning alone, as seen in [2]. (top) Compares the heating rates at 295K and a secular frequency of 660 kHz, (middle) at 295K and 1.3 MHz, and (bottom) at 4K and 1.3 MHz.

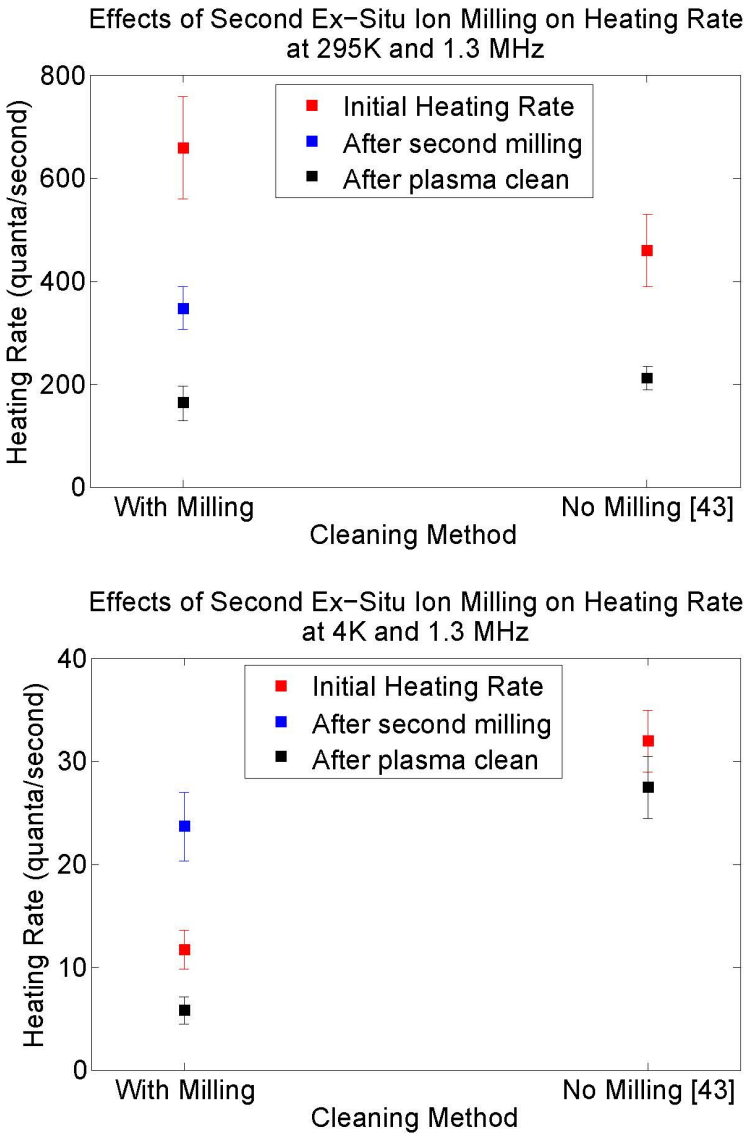

Figure 8-4: This figure compares heating rate reduction a second round of ion milling and plasma cleaning with the reduction from plasma cleaning alone, as seen in [2]. (top) Compares the heating rates at 295K and a secular frequency of 1.3 MHz, (bottom) at 4K and 1.3 MHz

son is a bit obscured because the initial heating rates from [2] are higher than those measured in our paper. This is likely due to a systematic uncertainty that is unaccounted for in our error analysis; this same uncertainty is reflected in the increase in the measured 4K heating rate after milling. Still, some conclusions can be drawn. A comparison between the initial and final heating rates from [2] shows no improvement in the heating rate at 4K and 1.3 MHz for plasma cleaning alone. Similarly, no improvement is seen after the first round of ion milling/plasma cleaning. Again, here the additional ex-situ milling is providing no additional advantage. In the measurements taken after the second round of milling, there is some small decrease in the final heating rate measurement. However, given the absence of improvement in any of the other data sets, it seems much more lilkely that this is symptomatic of the abovementioned systematic uncertainty than indicative of any true improvement in the heating rate.

8.3 Conclusion and Outlook

Cleaning our Nb trap chip via ex-situ ion milling combined with plasma cleaning did not offer a substantial improvement over using plasma cleaning alone. This experiment does not provide evidence for surface-restructuring as a mechanism by which ion milling reduces the anomalous heating rate seen by trapped ion experiments for Nb electrode surfaces.

However, this experiment was performed with a Nb trap, while the best ion-milling results were obtained by cleaning a gold trap. Furthermore, an experiment exploring the ex-situ milling of gold showed an intermediate improvment, where the heating rate was reduced by an order of magnitude [3]. This points to some difference between Nb and gold limiting the effects of ex-situ milling. A recent paper [48] suggests that a thin dielectric film (such as that formed by an metal oxide) can increase the magnitude of electric-field noise by several orders of magnitude. Niobium, unlike gold, forms such an oxide when exposed to air - this oxide would regrow after ex-situ milling. While ion milling would be able to remove such an oxide, our plasma cleaning would

not. To further explore the improvement mechanisms of cleaning via ion milling, the experiment should be repeated with a gold trap. We are currently pursing such experiments. Nonetheless, it is interesting to see a numm result in the case of Nb, highlighting the material differences tht may be playing a role once common surface contaminants are removed (as in e.g. plasma cleaning).

Bibliography

[1] D. Hite, Y. Colombe, A. Wilson, K. Brown, U. Waring, R. Jordens, J. Jost, D. Pappas, D. Leibfried, D. Wineland, and K. McKay. 100-fold reduction of electric-field noise in an ion trap cleaned with in sity argon-ion-beam bombardment. *Physical Review Letters*, 109:103001–1 – 103001–6, 2012.

[2] R. McConnell, C. Bruzewicz, J. Chiaverini, and J. Sage. Reduction of trapped ion anomalous heating by in situ surface plasma cleaning. *Physical Review A*, 92, 2015.

[3] K. McKay, D. Hite, Y. Colombe, R. Jordens, A. Wilson, D. Slichter, D. Allcock, D. Leibfried, D. Wineland, and D. Pappas. Ion-trap electrode preparation with ne^+ bombardment. 2014. arXiv:1406.1778.

[4] P. Shor. Algorithms for quantum computation: Discrete logarithms and factoring. *IEEE Symposium on the Foundation of Computer Science*, pages 124–134, 1994.

[5] D. DiVencenzo. The physical implementation of quantum computation. *Fortschr. Phys.*, 48:771–983, 2000.

[6] C. Ballance, T. Harty, N. Linke, M. Sepiol, and D. Lucas. Laser-driven quantum logic gates with precision beyond the fault-tolerant threshold. 2015. arXiv:1512.04600.

[7] J. Cirac and P. Zoller. Quantum computations with cold trapped ions. *Physical Review Letters*, 74:4091–4094, 1995.

[8] F. Schmidt-Kaler, H. Häffner, M. Riebe, S. Gulde, G. Lancaster, T. Deuschle, C. Becher, C. Roos, J. Eschner, and R. Blatt. Realization of the cirac-zoller controlled-not quantum gate. *Nature*, 422:408–411, 2003.

[9] L. Deslauriers, S. Olmschenk, D. Stick, W. Hensinger, J. Sterk, and C. Monroe. Scaling and suppression of anomalous quantum decoherence in ion traps. *Physical Review Letters*, 97, 2006.

[10] J. Chiaverini and J. Sage. Insensitivity of ion motional heating rate to trap material over a large temperature range. *Physical Review A*, 89, 2014.

[11] C. Moore. *Atomic energy levels*, volume 2. U.S. Government Printing Office, 1952.

[12] T. Dinneen, K. Vogel, E. Arimondo, J. Hall, and A. Gallagher. Cold collisions of sr*-sr in a magneto-optical trap. *Physical Review A*, 59:1216–1222, 1999.

[13] M. Baig, M. Yaseen, R. Alo, A. Nadeem, and S. Bhatti. Near-threshold photoionization spectra of strontium. *Chem. Phys. Lett.*, 296:403–407, 1998.

[14] A. Gallagher. Oscillator strengths of ca ii, sr ii, and ba ii. *Physical Review*, 157:24–30, 1967.

[15] H. Margolis, G. Huang, G. Barwood, S. Lea, H. Klein, W. Rowley, P. Gill, and R. Windeler. Absolute frequency measurement of the 674-nm $^{8}8sr+$ clock transition using a femtosecond optical frequency comb. *Physical Review A*, 67:032501–032505, 2003.

[16] V. Letchumanan, M. Wilson, P. Gill, and A. Sinclair. *Lifetime measurement of the metastable $4d^2D_{\frac{5}{2}}$ state in $^{8}8Sr^{+}$ using a single trapped ion*, volume 72. 2005.

[17] R. Blatt, G. Lafyatis, W. D. Phillips, S. Stenoln, and D. Wineland. Cooling in traps. *Physica Scripta*, 22:216–223, 1988.

[18] W. Itano and D. Wineland. Laser cooling of ions stored in harmonic and penning traps. *Physical Review A*, 25:35–54, 1982.

[19] D. Wineland, R. Drullinger, and F. Walls. Radiation-pressure cooling of bound resonant absorbers. *Physical Review Letters*, 40:1639–1642, 1978.

[20] D. Wineland and W. Itano. Laser cooling of atoms. *Physical Review A*, 20:1521–1540, 1979.

[21] D. Heinzen and D. Wineland. Quantum-limited cooling and detection of radio-frequency oscillations by laser-cooled ions. *Physical Review A*, 42:2977–2994, 1990.

[22] C. Monroe, D. Meekhof, B. King, S. Jefferts, W. Itano, D. Wineland, and P. Gould. Resolved-sideband raman cooling of a bound atom to the 3d zero-point energy. *Physical Review Letters*, 75, 1995.

[23] D. Wineland and H. Dehmelt. Proposed $10^{14}\delta\nu < nu$ laser flourescence spectroscopy on tl^{+} mono-ion oscilator iii (sideband cooling). *Bulletin of the American Physical Society*, 20:637, 1975.

[24] D. Wineland, W. Itano, J. Bergquist, and R. Hulet. Laser cooling limits and single-ion spectroscopy. *Physical Review A*, 36:2220–2232, 1987.

[25] W. Paul. Electromagnetic traps for charged and neutral particles. *Reviews of Modern Physics*, 62:531, 1990.

[26] J. Chiaverini, R. Blakestad, J. Britton, J. Jost, L. Langer, D. Leibfried, R. Ozeri, and D. Wineland. Surface-electrode architecture for ion-trap quantum information processing. *Quantum Information and Computation*, 5:419–439, 2005.

[27] G. Werth, N. Viorica, and G. Fouad. *Charged Particle Traps II: Applications*. Springer, 2009.

[28] P. Ghosh. *Ion Traps*. Oxford University Press, 1995.

[29] M. Brownnutt. *$^{88}Sr^{+}$ ion trapping techniques and technologies for quantum information processing*. PhD thesis, Imperial College London, 2007.

[30] E. Mathieu. Memoire sur le mouvement vibratoire d'une membrane de forme elliptique. *Journal de Mathematiques Pures et Appliquees*, 13:137, 1868.

[31] J. Wesenberg. Electrostatics of surface-electrode ion traps. *Physical Review A*, 78, 2008.

[32] M. House. Analytic model for electrostatic fields in surface-electrode ion traps. *Physical Review A*, 78, 2008.

[33] D. Hite, Y. Colombe, A. Wilson, D. Allcock, D. Leibfried, D. Wineland, and D. Pappas. Surface science for improved ion traps. *MRS Bulletin*, 35:826–833, 2014.

[34] J. Preskill. Reliable quantum computers. *Proc. Roy. Soc. Lond. A*, 454:385–410, 1998.

[35] A. Sorensen and K. Molmer. Entanglement and quantum computation with ions in thermal moiton. *Physical Review A*, 62, 2000.

[36] E. Knill. Physics: Quantum computing. *Nature*, 463:441, 2010.

[37] C.D. Bruzewicz, J. Sage, and J. Chiaverini. Measurement of ion motional heating rates over a range of trap frequencies and temperatures. *Physical Review A*, 91, 2014.

[38] M. Brownnutt, M. Kumph, P. Rabl, and R. Blatt. Ion-trap measurements of electric-field noise near surfaces. *Reviews of Modern Physics*, 87:1419, 2015.

[39] G. Hao Low, P. Herskind, and I. Chuang. Finite geometry models of electric field noise from patch potentials in ion traps. 2011. arXiv:1109.2995.

[40] D. Allcock, L. Guidoni, T. Harty, C. Ballance, M. Blain, A. Steane, and D. Lucas. Reduction of heating rate in a microfabricated ion trap by pulsed-laser cleaning. *Physics*, 13, 2011.

[41] N. Daniilidis, S. Gerber, G. Bolloten, M. Ramm, A. Ransford, E. Ulin-Avila, I. Talukdar, and H. Haffner. Probing surface electric field noise with a single ion. *Physical Review B*, 89, 2014.

[42] J. Chiaverini, A. Kerman, and J. Sage. Loading of a surface-electrode ion trap from a remote, precooled source. *Physical Review A*, 86, 2012.

[43] D. Berkeland, J. Miller, J. Bergquist, W. Itano, and D. Wineland. Minimization of ion micromotion in a paul trap. *Journal of Applied Physics*, 83:1147, 1998.

[44] D. Berkeland, D. Raymondson, and V. Tassin. Tests for non-randomness in quantum jumps. *Physical Review A*, 69, 2004.

[45] Siverns, Simkins, Weidt, and Hensinger. On the application of radio frequency voltages to ion traps via helical resonators. *Applied Physics B*, 106:327, 2012.

[46] D. Gandolfi, M. Niedermayr, M. Kumph, M. Brownnutt, and R. Blatt. Compact rf resonator for cryogenic ion traps. *Rev. Sci. Instrum*, 83, 2012.

[47] R. Matua. Electrical resistivity of copper, gold, palladium and silver. *J. Phys. Chem. Ref. Data*, 8:1147, 1979.

[48] M. Kumph, C. Henkel, P. Rabi, M. Brownnutt, and R. Blatt. Electric-field noise above a thin dielectric layer on metal electrodes. arXiv:1511.00624.